Title
Developing next generation quantum dot solids for photovoltaics

Author
Keene, Samuel

Publication Date
2018

Peer reviewed|Thesis/dissertation

UNIVERSITY OF CALIFORNIA,
IRVINE

Developing next generation quantum dot solids for photovoltaics

THESIS

submitted in partial satisfaction of the requirements
for the degree of

MASTER OF SCIENCE

in Physics

by

Samuel Thomas Keene

Thesis Committee:
Assistant Professor Shane Ardo, Chair
Chancellor's Professor Reginald M. Penner
Associate Professor Ilya Krivorotov

2018

Table of Contents

LIST OF FIGURES iii

LIST OF TABLES iv

ACKNOWLEDGMENTS v

ABSTRACT OF THE THESIS vi

1 Introduction 1

1.1 Theory and Motivation 1

1.2 Background 6

1.3 This Work 12

2 Developing QD heterostructures for enhanced carrier multiplication 14

2.1 Hot injection partial exchange reactions 14

2.1.1 CdSe Synthesis Procedures 14

2.1.2 Exchange Synthesis Procedures 16

2.1.3 Results and Discussion 17

2.2 Soution phase SILAR 20

2.2.1 SILAR Procedures 20

2.2.2 Results and discussion 22

2.3 ALD infilling with PbS 26

2.3.1 Reactor design 27

2.3.2 Characterization of PbS films 29

2.3.3 Characterization of PbS/CdSe films 31

2.3.4 Issues with PbS ALD 36

2.4 Conclusion 37

3 Charge transport studies in high performance PbS QD films 38

3.1 Film fabrication 38

3.2 Oxidation study using FETs 40

3.3 Carrier type determination using XPS/UPS 42

3.4 Conclusions 44

References 46

LIST OF FIGURES

Figure 1. Properties of synthesized CdSe QDs. 16

Figure 2. Absorption spectra of partially exchanged CdSe/PbSe QDs 18

Figure 3. TEM images of CdSe/PbSe QDs synthesized via cation exchange reaction 19

Figure 4. Cartoon of the solution-phase SILAR procedure 22

Figure 5. Absorption spectra of core/shell QDs prepared using solution-phase SILAR 23

Figure 6. TEM images of core/shell QDs grown via solution-phase SILAR 24

Figure 7. XRD pattern of CdSe QDs before and after one cycle of PbS SILAR 25

Figure 8. CdSe QDs before and after one PbS SILAR cycle 26

Figure 9. Schematic of the ALD reactor 29

Figure 10. Characterization of PbS films growth via ALD 30

Figure 11. I/V curves of FETs with ALD-grown PbS as the active layer 31

Figure 12. UV-vis spectra of CdSe QD films before and after PbS ALD 33

Figure 13. XPS depth profile results from CdSe-SCN films with PbS ALD 35

Figure 14. I/V curves of FETs fabricated using cation exchanged QDs 41

Figure 15. XPS and UPS measurements of cation exchanged QD films 43

LIST OF TABLES

Table 1. FET Mobility values.....40

ACKNOWLEDGMENTS

This work was completed over the course of the three years I spent working as a graduate researcher in Dr. Matt Law's lab. I acknowledge his financial support. The funding for the work was provided by the US Department of Energy as part of the Center for Advanced Solar Photophysics, an Energy Frontier Research Center.

I would like to thank my committee members for taking the time to participate in my advancement and eventual PhD defense and for taking the time to read this thesis. I would also like to thank my advisor Dr. Shane Ardo for taking me on as a graduate student as a fourth-year and for the support he has given me.

This work would not have been possible without the help and hard work of the LEXI staff scientists who kept the instruments running, helped me get the best data possible, and gave me guidance in designing my experiments. Thank you very much to Dr. Qiyin Lin, Dr. Jian-Gao Zheng, and Dr. Ich Tran.

Some of the most productive work on this project came as a result of collaborative efforts, so thanks to everyone at NREL and LANL and the rest of the EFRC for the great discussions and teamwork.

Lastly, thanks to all the people in the Law lab who made working there a little less miserable. Thanks Trenton, Jason, Zhongyue, Vineet, Moritz, Christian, Darren, Kan, Alex, Amanda, Nima, and Glen. And especially a huge thanks to Mark for training and mentoring me for my entire first year in the lab.

ABSTRACT OF THE THESIS

Developing next generation quantum dot solids for photovoltaics

By

Samuel Thomas Keene

Master of Science in Physics

University of California, Irvine, 2018

Professor Shane Ardo, Chair

Quantum dot photovoltaics have the potential to exceed theoretical efficiency limits of other photovoltaic devices and represent a potentially disruptive next-generation technology. In this thesis I present my efforts to develop and characterize novel quantum dot materials that have superior multi-exitonic, optical, and electronic properties. Several methods for the synthesis of inverse type-II core shell quantum dots are explored and their associated challenges are presented. A variety of materials characterization techniques are implemented to investigate these materials. Lastly, a collaborative investigation of the electronic properties of high performance lead sulfide quantum dots is presented.

1 Introduction

1.1 Theory and Motivation

A quantum dot (QD) is a semiconductor nanocrystal; it is an object with a single crystal structure whose size in all three dimensions is on the order of nanometers. Charge carriers in QDs are said to have various degrees of quantum confinement due to the size of the QD. In the limit of strong confinement, the electron and hole Bohr radii are much greater than the size of the QD and the carriers thus are forced into a much smaller space than they would normally occupy in the bulk material. Carrier-carrier interactions are greatly enhanced and excited electrons and holes can form as excitons due to their strong coupling. Strong confinement also has marked effects on electronic structure. In the simplest view of a bulk crystal, we formulate the density of states by considering free electrons subject to Born-von Karman boundary conditions over the entire crystal, resulting in an essentially continuous density of states proportional to the square root of energy:

$$g_{3D}(E) = \frac{3}{2}\frac{n}{E_F}\left(\frac{E}{E_F}\right)^{1/2}, \qquad E > 0. \tag{1}$$

In a QD, the electrons are not free in any dimension, and instead lie in a potential well. Allowed energies in this scenario are discrete, and thus the density of states is discrete as well:

$$g_{0D}(E) = 2\sum_{n_x,n_y,n_z} \delta\left(E - E_{n_x,n_y,n_z}\right). \tag{2}$$

This picture is quite simplistic, but its prediction of the discretization of transitions in QDs is in fact experimentally observed.

The electronic structure of strongly confined QDs can be modeled using $k \cdot p$ theory in the envelope function formalism. In a bulk crystal, $k \cdot p$ theory considers Bloch waves in the periodic lattice potential:

$$\left(\frac{p^2}{2m} + V\right) \mathrm{e}^{\mathrm{i}\boldsymbol{k}\cdot\boldsymbol{r}} u_{n\boldsymbol{k}}(\boldsymbol{r}) = E(\boldsymbol{k}) \mathrm{e}^{\mathrm{i}\boldsymbol{k}\cdot\boldsymbol{r}} u_{n\boldsymbol{k}}(\boldsymbol{r}). \tag{3}$$

Using the operator form of the momentum: $\boldsymbol{p} = -i\nabla$ we can rewrite (3) as

$$\left(\frac{p^2}{2m} + \boldsymbol{k}\cdot\boldsymbol{p} + \frac{k^2}{2m} + V\right) u_{n\boldsymbol{k}} = E_{n\boldsymbol{k}} u_{n\boldsymbol{k}}. \tag{4}$$

The k dependent terms are treated as a perturbation about a band extremeum $\boldsymbol{k} = \boldsymbol{k_0}$ using the complete set of orthonormal eigenfunctions $u_{n\boldsymbol{k_0}}$ of the unperturbed Hamiltonian as a basis[1]:

$$\left(\frac{p^2}{2m} + V\right) u_{n\boldsymbol{k_0}} = E_{n\boldsymbol{k_0}} u_{n\boldsymbol{k_0}}. \tag{5}$$

The second order perturbation gives an effective mass:

$$\left(\frac{m}{m^*}\right) = \delta_{\mu\nu} + \frac{2}{m} \sum_{m\neq n} \frac{< n0|p_\mu|0\delta >< \delta 0|p_\nu|0n >}{E_{n\boldsymbol{k_0}} - E_{m\boldsymbol{k_0}}}, \tag{6}$$

where μ and ν are the principal axes, and a dispersion relation:

$$E_n(\boldsymbol{k}) = E_{n\boldsymbol{k_0}} + \sum_{\mu,\nu} \frac{1}{2m} \left(\frac{m}{m^*}\right)_{\mu\nu} k_\mu k_\nu. \tag{7}$$

In a typical calculation for a semiconductor, degenerate perturbation theory is used for degenerate bands, spin-orbit coupling is considered, and the conduction and valence bands are treated as quasi-degenerate, yielding the well-established 6- and 8-band $k \cdot p$ models[2,3].

In a QD, there is still a crystal lattice so the $k \cdot p$ formalism still applies, but with the added constraint of quantum confinement. The full Hamiltonian is now

$$[H_{1e} + \bar{V}(\boldsymbol{r})]\psi(\boldsymbol{r}) = \epsilon\, \psi(\boldsymbol{r}) \tag{8}$$

where H_{1e} is the Hamiltonian in (3) corresponding to the crystal lattice and $\bar{V}$ is the non-periodic potential corresponding to the quantum confinement of the nanocrystal. A simple, but successful model uses the infinite square well potential for $\bar{V}$.[4] This simply requires $\psi(\boldsymbol{r})$ to go to zero at the boundaries, which is achieved by casting it as a linear combination of Bloch waves times a set of "envelope functions"

$$\psi(\boldsymbol{r}) = \sum_{n,\boldsymbol{k}} F_{n,\boldsymbol{k}}(\boldsymbol{r})\phi_{n,\boldsymbol{k}}(\boldsymbol{r}). \tag{9}$$

Where the Bloch waves $\phi_{n,\boldsymbol{k}}(\boldsymbol{r}) = \mathrm{e}^{\mathrm{i}\boldsymbol{k}\cdot\boldsymbol{r}} u_{n,\boldsymbol{k}}(\boldsymbol{r})$ are those of the 6 or 8 bands at the band extrema. $k \cdot p$ theory in the envelope function formalism has been successfully applied to QD systems in the strong confinement regime, yielding the energy spectrum, wavefunctions, dipole transition states and selection rules[5]. The predicted discrete absorption and emission energies agree well with experiment, although the transition lines in actual samples are broadened due to finite size distributions. One of the most striking features of the QD electronic structure is a size-dependent increase in the bandgap, which is referred to as the confinement energy.[6] The ability to tune the bandgap with QD size and the existence of discrete transition lines are two of the most attractive feature of strongly confined QDs as a semiconductor material.

Strong carrier confinement also results in increased coulomb interaction between charge carriers due to their localization. Carrier-carrier interactions such as Auger recombination and impact ionization (I.I.), which do not contribute appreciably to dynamics in bulk semiconductor devices, are thus greatly enhanced. In an Auger process, two electrons (holes) in the conduction (valence) band interact via the coulomb interaction; one relaxes to the valence (conduction) band and the other is promoted to a further excited state with energy at least twice the band gap energy E_g (the carrier is now a "hot" carrier). I.I. in the reverse process: a single hot carrier gives up energy E_g to another carrier, promoting it to the excited band and thus increasing the number of excited carriers by one. Using the conduction and valence band wavefunctions calculated from $k \cdot p$ or any other suitable solid state theory, one can treat the coulomb interaction as a perturbation and write down its matrix element:

$$U_{if} = \int\int [\phi_1^*(\boldsymbol{r}_1)\phi_2^*(\boldsymbol{r}_2)\Delta_{21} - \phi_2^*(\boldsymbol{r}_1)\phi_1^*(\boldsymbol{r}_2)\Delta_{12}] \times [e^2 \exp(-\lambda r_{12})/\epsilon\, r_{12}]\phi_1'(\boldsymbol{r}_1)\phi_2'(\boldsymbol{r}_2)\, d\boldsymbol{r}_1\, d\boldsymbol{r}_2. \quad (10)$$

Here 1 and 2 are the carrier indicies, unprimed states are the initial states, primed states are the final states, λ is the screening length in the material and Δ_{21} and Δ_{12} are spin terms that are zero or one depending on the spin configurations of the initial and final states. Using Fermi's golden rule, it can then be shown[7] that if the perturbation is turned on at time zero, the probability of transitioning from state $|i\rangle$ to state $|f\rangle$ at time t is

$$T_{if} = (2t^2|U_{if}|^2/\hbar^2)[(1-\cos x)/x^2] \quad (11)$$

where $x = (t/\hbar)\left|E_f - E_i\right|$. If $\theta(r)$ is the probability of occupation or vacancy (determined by the process) for $r = 1, 1', 2, 2'$ in a given process, and $\rho(r)$ is the probability associated with the reverse process, then the net probability of the process occurring after time t is

$$P(t) = \int [\theta(1)\theta(1')\theta(2)\theta(2') - \rho(1)\rho(1')\rho(2)\rho(2')]T_{if}\, dS \qquad (12)$$

Where the integral is taken over all initial and final states.

The strong enhancement of Auger recombination and I.I. in quantum confined systems is evident in the $\exp(-\lambda r_{12})/r_{12}$ term in the matrix element. If there is a large population of hot carriers in such a system, it is expected that the rate of I.I. would be high. By far the greatest limitation on efficiency in a conventional photovoltaic device is the loss of hot electron energy to the lattice; regardless of incident energy, the most energy a single photon can contribute to the device is roughly E_g[8]. If all of the hot electrons in a device can be made to contribute multiple free carries via I.I, the theoretical efficiency limit on a device is drastically increased from 31% to nearly 45% for a single junction solar cell under one sun illumination[9]. Solar cells utilizing strongly confined QDs as the absorber layer are thus a fascinating area of research. In a QD the situation is slightly different because the electron-hole pairs are coupled and not separate as in the above consideration. I.I. in QDs is thus often referred to as multiple exciton generation (MEG). QDs also benefit from having reduced hot carrier cooling rates due to the lower density of phonon states resulting from the small crystal size[10] and from the relaxation of momentum conservation in Auger processes[11]. The hot exciton dynamics in QDs and their differences from bulk materials are an ongoing field of study. Extracting multiexcitons as useful current is a delicate task because Auger recombination and MEG have the same matrix element and therefore systems with high MEG rates will also lose just as many excitons to Auger recombination.

MEG can thus only enhance the efficiency of a solar cell if multiexcitons are separated into free carriers before they can undergo Auger recombination.

The lead chalcogenides (PbX; X = S, Se, Te) have large electron, hole and exciton radii ($a_{exciton} = 18, 46, 150$ for PbS, PbSe, PbTe, respectively), so PbX QDs, which can be synthesized with diameters on the order of 5 nm, lie in the strong confinement regime[12]. The range of bandgaps easily accessible for PbX QDs is roughly 0.5 to 1.5 eV, which encompasses the ideal bandgap for a conventional solar cell and a maximally MEG-enhanced solar cell. The lead chalcogenides, which adopt a rock salt structure, are direct bandgap materials are thus absorb strongly above the bandgap. PbX QDs can be synthesized colloidally, meaning PbX QD solar cells can be solution processed, presenting the possibility for low-cost roll-to-roll fabrication. PbX QDs have thus received considerable attention as absorber materials for high-efficiency, cheap solar cells.

1.2 Background

There exist synthesis methods for QDs of numerous materials, shapes, and sizes[13]. The most common synthesis route for PbX and many other common QDs is the "hot injection" method[14]. In a typical PbX QD synthesis, a selenium-phosphine complex such as TOPSe is injected into a heated solution of a lead-fatty acid complex such as lead oleate, in a non-coordinating solvent such as octadecene. In phosphine-based syntheses, a secondary phosphine such as diphenylphosphine can be used to increase reaction yield[15]. Reactions are carried out under air-free conditions using Schlenk techniques, and PbX QDs are typically processed in air-free environments to avoid oxidative effects. QDs are precipitated and washed several types to remove excess ligands, solvent, and reactants, and the resulting QDs

can be resuspended in non-coordinating solvent, stabilized by the long organic ligands used in the reaction.

Thin films of QDs are typically deposited by either layer-by-layer dip-coating or by single layer spin-coating. Films of QDs capped with oleate or other long organic ligands exhibit poor charge transport and are thus not suitable for use in solar cells or other devices. These ligands must therefore be removed at some point during the film deposition process without sintering the QD or otherwise eliminating their quantum confinement. This is achieved by exchanging them with short-chain organic ligands that yield conductive films. In a layer-by-layer process, substrates are sequentially dipped in QD solutions followed by ligand solutions, ensuring that each deposited layer has its ligands swapped. Spincast films must be treated with a ligand solution with sufficiently high concentration and time such that the entire film undergoes the ligand exchange process. In addition to improving transport, the choice of ligand can tune the properties of the QD by changing the band positions and Fermi level[16]. Recently, solution-based ligand exchange processes have been demonstrated on PbX QDs in which ligands are exchanged while maintaining QD colloidal stability[17]. This approach is attractive because films can be deposited in a single step without the complications of post-deposition treatment. Inorganic ligands have also received recent attention and a wide variety of ligands have been developed for numerous types of QD[18]. Ligands such as S^{2-} are smaller than even the smallest organic ligands such as hydrazine and therefore increase electronic coupling between QDs which enhances charge transport.

As-synthesized QDs exhibit air-instability in their optical and electronic properties[19]. Recently, synthetic routes have been developed to produce PbX QDs with improved air-stability. The incorporation of halide precursors into QD reactions has led to QDs whose

optical properties do not change after long periods of air exposure[20]. Instead of the canonical lead oleate precursor, a mixture of lead-halide salt in oleylamine is used. The presence of halides on the surface of the dots is verified using XPS. These QDs have been used to fabricate solar cells that have minimal performance reduction after air exposure. Post-synthesis halide treatment has also been demonstrated to improve stability and device efficiency[21]. Solutions of oleate-capped QDs are exposed to halides either through mixing with solutions of halide salts such as tetrabutylammonium iodide (TBAI), or by exposure to elemental chlorine[22]. Yet another form of halide passivation involves a hot injection of CdX QDs into a lead-halide/oleylamine mixture that causes a near-complete exchange of Cd with Pb, with similar results to the direct halide-based synthesis[23]. Increases in post-treatment PL lifetime suggest that halide treatment reduces the density of trap states; DFT calculations support the same hypothesis[24]. The exact mechanism and effect of halide treatment is an ongoing area of study.

Another effective QD passivation technique is solid-state infilling of a metal-oxide matrix via atomic layer deposition (ALD). In addition to making PbX QDs air-stable, ALD of amorphous alumina has been shown to increase carrier mobility and enhance device performance[25]. Combining ALD with short, inorganic ligand exchange treatments has resulted in field effect transistors (FETs) with high electron mobilities[26]. ALD has also been shown to enhance MEG in QD thin films[27]. As-synthesized QDs have surface trap states caused by impurities, defects, and ligands. Trap states generally reduce performance in devices and are the source of unwanted time-dependent responses such as the bias stress effect[28]. Removing the ligands or replacing them with inorganic species, then infilling with an inorganic matrix effectively passivates all or most of these traps. The reduced inter-dot distance from exchanging the ligands results in greater mobility, so the ligand exchange/ALD

combination improves transport both through trap passivation and through improved electronic coupling.

Although there were initially conflicting measurements of MEG rates in QDs, discrepancies were eventually attributed to sample photocharging and improved experimental design was developed to measure only true MEG events[29]. MEG in isolated QDs is typically measured using ultrafast techniques, such as transient absorption or time-resolved photoluminescence spectroscopy. In either approach, a colloid of constantly stirred QDs is excited with a femtosecond laser pulse with energy at least twice the QD band gap. The pulse fluence must be low enough as to not excite multiple excitons per pulse. The occupation of the band-edge states is then measured as a function of time. Single excitons and biexcitons decay with different time constants, so the signal can be fit to extract both the biexciton lifetime and the overall quantum efficiency. PbX QDs show an onset of MEG at around $2.7E_g$ with the highest quantum yield vs. excitation energy for PbTe and lowest for PbS[30]. Because the measured biexciton lifetimes are the same for PbS, PbSe, and PbTe QDs, the MEG enhancement down the chalcogenide group is attributed to slower carrier cooling due to better dielectric screening; the trend indeed matches the trend in dielectric constant with $\varepsilon = 17, 23, 33$ for PbS, PbSe, PbTe respectively[31]. PbSe nanorods with aspect ratios of 6-7 have been shown to have higher MEG efficiencies and lower MEG throesholds ($2.5E_g$) than PbSe QDs, which is attributed to slower cooling due to charge separation[32]. Larger aspect ratios do not yield as high quantum efficiencies; the hypothesis is that greater restrictions on momentum conservation in longer rods reduce the MEG rate. A further increase in quantum efficiency and MEG thresholds approaching the theoretical limit of $2E_g$ has been observed in PbSe/CdSe core/shell QDs, which adopt a quasi-type-II band

alignment[33]. In these heterostructures, excited electrons are delocalized across the entire nanocrystal while excited holes are confined to the core, increasing charge separation, decreasing phonon density of states for holes, increasing hole-hole interactions, and thus greatly slowing carrier cooling while simultaneously enhancing MEG.

Carrier dynamics in QD thin films vary considerably from isolated QDs in suspension. MEG-enhanced solar cells require that multiexcitons are still produced at a high rate after film processing and also that they are successfully separated and extracted. The process of generating two or more excitons from a single photon and subsequently dissociating it into free charge carriers is termed Multiple Free Charge Generation (MFCG). MFCG can be measured in QD thin films using time-resolved microwave conductivity (TRMC) measurements, in which the absorption of microwave radiation is measured with respect to time following excitation by an ultrafast laser pulse. This technique does not require the use of electrodes and avoids complications from photocharging[34]. TRMC has been used to demonstrate that MFCG in PbSe QD thin films has a strong dependence on carrier mobility[35]. By varying ligand length and capping group, QD films spanning the mobility range of roughly 0.01 to 1 $cm^2/(V{\cdot}s)$ were deposited. MFCG efficiency increased with carrier mobility, up to a maximum of nearly 40% for films with 1,2-ethandiamine (2DA) ligands ($\mu \approx 1 cm^2/(V \cdot s)$). Carrier mobility was also varied by infilling films with Al_2O_3 using ALD, yielding films with mobilities similar to the 2DA films[36]. The MFCG rates were nearly identical, indicating that mobility is a key parameter in the efficient separation and extraction of multiexcitons. Remarkably, all films studied showed an MEG onset very close to $2E_g$. It is still unclear what causes the decrease in MEG threshold when QDs are assembled in a film.

The first working quantum dot solar cells were built with simple Shottky junction[37] and p-n heterojunction geometries[38]. The heterojunction geometry was quickly adopted by the field due to its potential for higher efficiency devices. A typical device stack, consists of a conductive oxide, such as indium-tin-oxide (ITO), on glass, a sputtered or nanocrystalline oxide window layer such as ZnO or TiO_2, a film of QDs deposited by drop-casting, spin-coating or dip-coating, and evaporated metal contacts. Device efficiencies were improved by employing an electron-blocking MoO_3 layer between the contacts and the QD film[39]. Almost all reported QD devices above 5% power conversion efficiency (PCE) have used PbS QDs as the absorber layer.

The most efficient devices to date have incorporated some form of halide treatment with band position engineering to increase charge separation. Halide treatment not only makes the devices air stable, but also seems to enhance efficiency in the wide variety of device architectures in which it is utilized. One successful strategy has been to change the ligand partway through the QD layer. The QDs in contact with the ZnO window layer are capped with TBAI while those in contact with the metal contacts are capped with ethanedithiol (EDT)[40]. Changing the ligand solution partway through dip-coating deposition ensures a smooth interface. The band alignment of the device stack separates charge in a similar way to the utilization of MoO_3, but is potentially more effective because the band positions of MoO_3 are extremely sensitive to stoichiometry and thus the deposition method. Heterojunction QD devices have been fabricated that also two different ligand treatments to fabricate both *n* and *p* type QDs[41].

One of the widespread limitations of even the state-of-the-art QD solar cells is low quantum efficiency near the band edge. The absorption coefficient of the QD layer is lower

in this region of the spectrum because of band-tailing due to polydispersity and other forms of irregularity such as native defects and inhomogeneity of ligand exchange, meaning that photons penetrate deeper into the film. Low quantum efficiency means that carrier separation and extraction at the back metal contact is poor, and that transport in the QD layer is limited. State of the art PbS devices use fully solution processed ligand exchange in conjunction with halide treatment to reduce inhomogeneity, passivate the QD surfaces, and provide air stability, allowing them to achieve over 11% PCE[42]. New QD materials such as $CsPbI_3$ have also been developed and have achieved the highest efficiency for any QD solar cell at 13.4%, although these materials have low Bohr radii and MEG in these QDs is not enhanced compared to bulk[43].

Although the most efficient QD solar cells have been fabricated with PbS, the potential for MEG enhancement in PbSe and PbTe devices is much greater. The high instability of PbTe has prevented it from being used in devices, and the number of reported PbSe devices is much lower than that for PbS. However, an air-stable, 6% efficient PbSe device that utilized the lead-halide synthesis was recently reported[23]. Additionally, the first QD solar cell to clearly demonstrate MEG was fabricated using PbSe and a combination of EDT and hydrazine ligand treatment[44]. The peak external quantum efficiency (EQE) in these devices was 114%, and the MEG onset (lowest energy with EQE > 100%) occurred at $2.8E_g$. The demonstration of MEG in a QD solar cell was a major milestone in the field, but MEG has to be greatly enhanced to contribute substantially to PCE.

1.3 This Work

The two major advances in QD solar cells have been air stability (a major step forward) and increased efficiency. Gains in efficiency have come from a variety of

processing techniques, but there are still major problems with QD devices that must be addressed; low band edge EQE and the lack of a depletion region in heterojuction devices are two good examples. Further characterization of QD materials that already are implemented in relatively high efficiency solar cells should give insight into these limitations.

The other area of QD solar cells that can be majorly improved is the structure of the QDs themselves. MEG rates in quasi type-II PbSe/CdSe core/shell nanocrystals have already been measured to be much higher than even PbTe QDs; PbSe nanorods have also been shown to have higher MEG rates than spherical QDs. Applying the core/shell structure to nanorods could result in even higher MEG rates. The problem with PbSe/CdSe core-shells is that using the shallower valence band PbSe as the core material confines excited holes to the core which kills transport in a thin film. The reversed structure – a CdX/PbX core/shell – combined with inorganic ligand exchange and alumina ALD should result in QD thin films with excellent transport properties and high MEG rates. In the optimal device stack, these thin films can be the absorber layer in record efficiency QD solar cells. No CdX/PbX nanocrystals have been synthesized, but there are several potentially successful approaches, such as partial ion exchange reactions, solution-phase shell growth[45], and ALD of PbS on a film of CdSe QDs.

In this thesis I will describe my efforts in each of these areas of research and present my progress, limitations, and perspective going forward.

2 Developing QD heterostructures for enhanced carrier multiplication

The purpose of this project was to develop inverted quasi type-II QDs suitable for use in solar cells. The CdX/PbX core/shell system was selected for a number of reasons, including: CdSe core QDs are easy to synthesize, the overall system has good optical absorption, the reverse system PbX/CdX is the most widely studied core/shell QD system for MEG, and CdX and PbX crystal structures have small lattice mismatch and both have cubic crystal structures. Two solution phase approaches were explored: hot-injection partial exchange, and solution phase successive ionic layer adsorption reaction (SILAR) which is also referred to as colloidal ALD. A CdSe/PbS inorganic matrix approach was also explored, in which ALD was used to attempt to grow a PbS matrix around a ligand-free thin film of CdSe QDs. A variety of techniques were used to characterize the resulting samples, including UV-vis spectroscopy, scanning electron microscopy (SEM), transmission electron microscopy (TEM), FET measurements, X-ray photoelectron spectroscopy (XPS), and X-ray diffraction. The ALD approach was overall the most promising, but limitations involving the ALD precursor and reactor made sample reproducibility a challenge.

2.1 Hot injection partial exchange reactions

2.1.1 CdSe Synthesis Procedures

Both the hot-injection and SILAR synthesis approaches require CdSe QD cores as starting materials. An ideal synthesis method should be facile, require stable and inexpensive precursors, be scalable to large batch sizes, be flexible enough to synthesize a wide range of QD sizes, produce QDs with low (<5%) polydispersity, and produce stable QDs. The method published by Peng et al was selected because it satisfies these criteria[46]. The procedure is briefly described below:

4 mmol (0.512 g) CdO, 20 mmol (6.28 g) oleic acid (OA), and 25 g 1-octadecene (ODE) are combined in a 100 mL 3-neck round-bottom flask. The flask is degassed below 50 mtorr and then refilled with Ar three times at 100 C to remove all dissolved oxygen and remove water. The mixture is raised to 260 C for roughly 30 min in order to react CdO with OA to form cadmium oleate. The solution should be clear or pale yellow at this point and no trace of red CdO should be present. The solution is then raised to 270 C. Meanwhile, the selenium precursor is prepared in a nitrogen glovebox by adding 4 mmol Se powder (-200 mesh) to 10 mL ODE. The mixture is vigorously shaken to suspend the Se and then immediately loaded into a syringe. The Se precursor is injected into the round-bottom flask and the flask is maintained at 240 C for 10 min. The flask is then allowed to cool in air until it reaches approx. 150 C, at which point it is safe to cool in an ice bath to room temperature without breaking the flask. The flask is then brought into the glovebox to wash the QDs. Washing can be done in air, but subsequent work with these QDs was frequently done air-free, so washing was done under nitrogen using anhydrous solvents. The QDs are precipitated using EtOH and centrifuged at 4400 rpm for 5 min. The supernatant is discarded and the QDs are resuspended in hexane. This procedure is performed three times to remove all unreacted precursors. The QDs are then dried in the glovebox antechamber for roughly 30 min. The resulting QDs can be suspended in hexane, octane, tetrachloroethylene, or another desired nonpolar solvent, or stored dry. This procedure produces CdSe QDs that are 3.5 nm in diameter, have a first exciton absorption peak at 525 nm, and adopt the zinc-blende crystal structure, as shown in the representative UV-vis, TEM and XRD data in Figure 1.

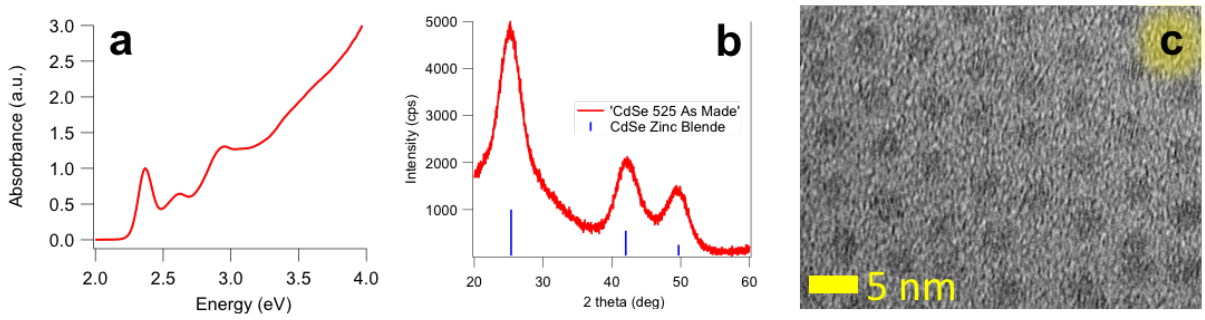

Figure 1. Representative absorbance spectrum (a), XRD pattern (b) and TEM image (c) of as-synthesized CdSe QDs with first exciton peak at 525 nm. QDs adopt the zinc-blende crystal structure and have an average size of 3.5 nm with a narrow size distribution.

In order to synthesize smaller QDs, 10 mmol OA is used and the reaction temperature is reduced. The reaction yield decreases as the temperature decreases, and the lowest temperature explored was 200 C, which yields 2 nm QDs with first exciton peak at 430 nm. Larger QDs can also be synthesized by halving the Se precursor injection and then adding 2 mmol of trioctylphosphine-selenide (TOP-SE) dropwise to the flask. The maximum size is 4.5 nm with first exciton peak at 600 nm.

2.1.2 Exchange Synthesis Procedures

The first attempted method to synthesize CdSe/PbSe core/shell QDs was to modify an existing synthesis procedure that completely exchanges Pb for Cd in pre-synthesized CdSe QDs[23]. By decreasing reaction time and temperature and quenching the reaction rapidly, the goal was to arrest the exchange process before it was complete, and thus end up with QDs with Pb on the surface and Cd on the inside.

The exchange reaction procedure is as follows: first, CdSe QDs are synthesized via the procedure outlined in the previous section and suspended in ODE in a 50 mg/mL concentration in the glovebox. 3 mmol $PbCl_2$ and 10 mL oleylamine (OLA) are added to a

round bottom flask and degassed three times at 80 C and the heated to 140 C under argon for 30 min. The temperature is set to the desired reaction temperature and 5 mL of the QD suspension is swiftly injected into the flask. The reaction is then immediately quenched in liquid nitrogen. The cation exchange happens almost instantaneously, as evidenced by an immediately color change from yellow/orange/red (repending on CdSe size) to dark brown, thus it is important to quench the reaction as quickly as possible. The flask is then brought into the glovebox and the solution is centrifuged once to separate excess $PbCl_2$ from the rest of the solution. Washing is then performed as described in the previous section. This procedure was conducted at reaction temperatures of 170 C, 140 C, 120 C, 100 C, and room temperature and the resulting QDs were measured using UV-vis and TEM.

2.1.3 Results and Discussion

Figure 2 shows the absorption spectra of each sample after cation exchange compared to the starting CdSe QDs. The 170 C reaction temperature achieves complete cation exchange and the results matched published results for completely exchanged QDs. As the temperature is decreased, the exciton peak in the near IR that corresponds to PbSe shifts to higher energy, indicating that the amount of Pb incorporated into each QD is smaller (a smaller PbSe domain results in a higher energy peak). The original CdSe exciton peaks are not evident in any of the samples, although the extremely strong absorption of PbSe in this spectral region makes it difficult to make conclusions about the CdSe from UV-vis measurements alone. The definition of the PbSe peak decreases as the reaction temperature is decreased, indicating a wider range in the size of PbSe domain. The room temperature sample has no near IR exciton peak; the original CdSe spectrum is instead completely washed-out.

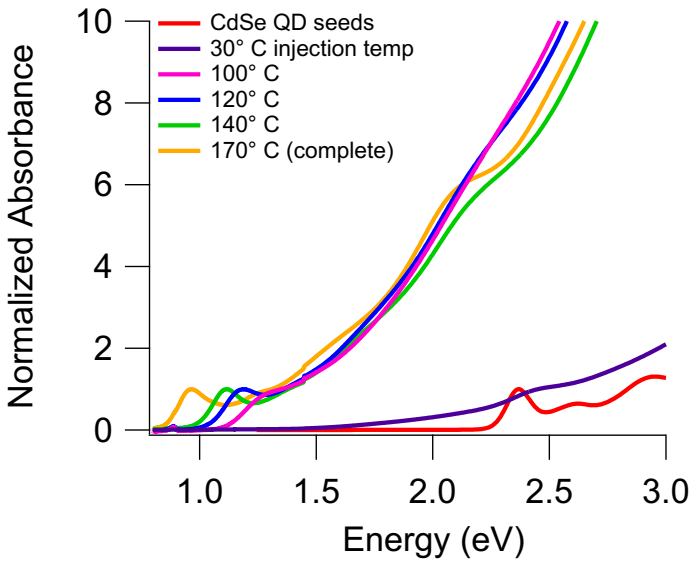

Figure 2. Absorption spectra of partially exchanged CdSe/PbSe QDs compared to starting CdSe QDs and completely exchanged PbSe QDs. As reaction temperature is decreased, the amount of of Pb incorporated into the QDs decreases, as evidenced by the shift of the near IR exciton peak towards higher energy (smaller size).

Figure 3 shows TEM images of samples synthesized at 170 C, 120 C, and room temperature. Any of the samples in the 100-170 C range look very similar; they remain individual QDs with no change in size. However, there are isolated instances of QDs in the images for lower reaction temperatures that appear to only have lattice fringes over a portion of the QD, indicating two different crystal structures. Two of these instances are pointed out in the 120 C image. Combined with the UV-vis results, these data are strongly indicative that heterostructured CdSe/PbSe QDs are being formed. At room temperature, the QDs simply agglomerate, so it appears that roughly the 100-120 C range is ideal for forming stable heterostructures.

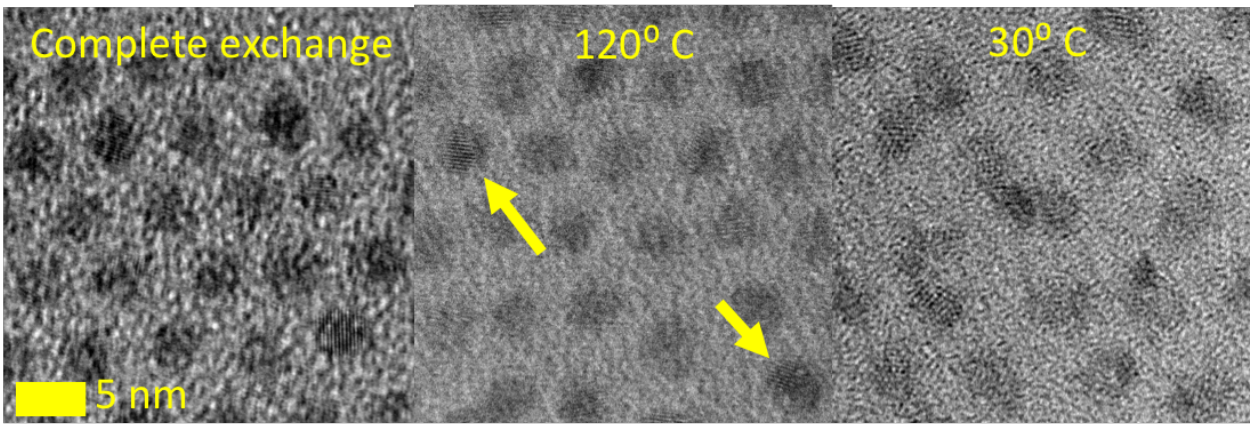

Figure 3. TEM images of CdSe/PbSe QDs synthesized via cation exchange reaction at 170 C (left), 120 C (right), and room temperature (right). The 170 C reaction temperature results in complete exchange. The 120 C reaction temperature appears to result in partial exchange; the highlighted QDs in the image have lattice fringes over only a portion of their area. The room temperature reaction causes the QDs to aggregate.

Although these results were promising, at the time of this work UCI did not possess the advanced TEM imaging and atomic resolution elemental analysis capabilities that it now does, and so further characterization of the structure of these QDs was not possible. However, several of our collaborators also investigated the partial exchange reaction and conducted a mechanistic study of how the exchange reaction proceeds[47]. They found that the cation exchange begins at a [111] facet on the CdSe QDs and then propagates linearly across the QD. Thus the resulting heterostuctures are not core/shell structures but instead half-and-half "Janus particles." While suspensions of these particles did show comparably high MEG rates to PbSe/CdSe core/shell particles, they are not suitable for devices because there is no conductive pathway when they are organized into thin films because the lower bandgap PbSe halves are randomly oriented and there is no long-range pathway. Electronic measurements by our collaborators confirmed this. Because of the results of this investigation, we decided to explore other methods of CdSe/PbSe core/shell QD synthesis.

2.2 Solution phase SILAR

The next core/shell synthesis procedure that was explored was solution-phase layer-by-layer growth method based on a successive ionic layer adsorption reaction (SILAR). In this method, core CdSe QDs are sequentially exposed to cationic and anionic precursors to build up a layer of shell material. The QDs are kept separate from the precursors by maintaining a biphasic solution consisting of nonpolar and high dielectric constant aprotic solvents. The procedure generally involves keeping the QDs and the precursors in separate phases and vigorously stirring them together to expose the QDs to the precursors. The phase containing the precursor can then be easily removed and thus there is no unreacted precursor present when the next step is performed. This prevents uncontrolled growth of homogeneous material. This approach was based upon a successful literature report on the synthesis of CdSe/CdS core/shell QDs using SILAR in biphasic solution[45].

2.2.1 SILAR Procedures

CdSe QDs with first exciton peak at 525 nm, synthesized as described in Section 2.1.1, were used as the core particles for this work. Additionally, some TEM samples were made using 5 nm diameter, 600 nm first exciton QDs because they are much easier to image. There was no difference in results between these two QD starting materials. All experiments were conducted in a nitrogen glovebox using anhydrous solvents.

The first samples prepared were CdSe/CdS QDs – this was done in order to verify that we could reproduce the published results using this method. 1 mL toluene and 1 mL formamide (FAm) are added to a vial. These solvents are immiscible and form a biphasic solution. 200 μL of 20 mg/mL QD/toluene solution and 15 μL OLA are added to the toluene phase. 30 μL of 0.1 M Na_2S/FAm solution are added to the FAm phase and the entire

mixture is vigorously stirred for 10 min. The stirring should be vigorous enough to mix the two phases together and expose the QDs to the Na_2S solution. Alternatively, the vial can simply be shaken. The mixture is then allowed to rest to allow the phases to separate; this can be accelerating by centrifugation. The QDs are now coated by a layer of sulfide and are stabilized by the OLA ligands. The FAm phase is discarded and the solution in rinsed twice with fresh FAm to ensure all residual precursor is removed. After discarding the FAm after each rinse, 1 mL of fresh FAm is added along with 30 μL of 0.1 M Cd-acetate/FAm solution. The entire mixture is stirred, allowed to rest, and rinsed as before. The QDs are now coated by a layer of CdS and are still stabilized by the OLA ligands. This procedure can be repeated to grow as many layers of CdS as are desired. The QDs can then be precipitated with MeOH and centrifuged and either resuspended in nonpolar solvent or stored dry. The resulting QDs are extremely emissive (they glow in room light) which is indicative of the type-I CdSe/CdS core/shell band alignment.

Once this procedure was verified with CdSe/CdS QDs, the process was altered to use Pb precursors. For the samples characterized in the following section, the exact procedure as above was used except Cd-acetate was replaced by Pb-acetate. After the first full cycle the QD solution makes a distinct color change to dark red and appears to be colloidally stable. After subsequent cycles, the solution becomes dark brown and while some material stays in suspension, some begins to precipitate. The precipitate was typically discarded; XRD analysis showed that it was bulk PbS.

Additionally, numerous other combinations of solvents and precursors were attempted. All permutations of the following were attempted, with either similar or worse results: N-methyl formamide and N-N-dimethyl formamide were used as nonpolar

solvents; didodecyldimethylammonium bromide was used as a ligand; Pb-oleate was used as a Pb precursor; NH_4S was used as a sulfur precursor; Na_2Se and Na_2Te were used as selenium and tellurium precursors instead of sulfur precursors. Most of the experiments were done with sulfur precursors because of the cost and instability of the selenium and tellurium precursors, however these precursors were attempted to ensure that they did not have superior results. A schematic of the procedure is shown in Figure 4.

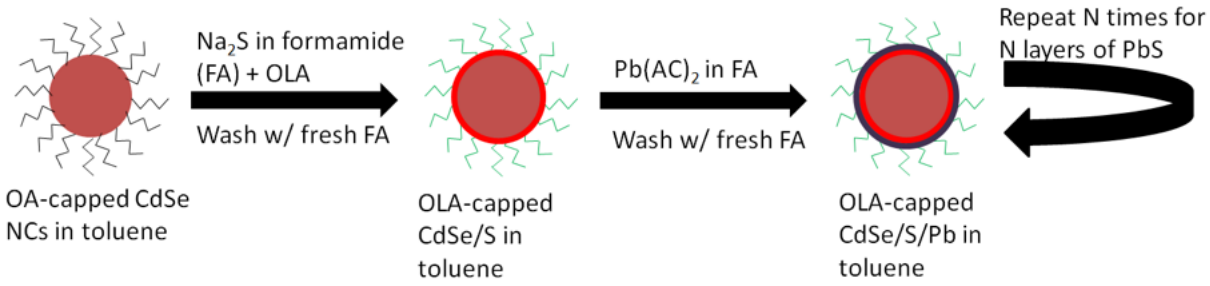

Figure 4. Cartoon of the solution-phase SILAR procedure

2.2.2 Results and discussion

Optical absorption spectra of CdSe/CdS and CdSe/PbS QDs prepared via solution-phase SILAR are shown in figure 5 for a range of SILAR cycles. The CdSe exciton peaks in the CdSe/CdS samples are preserved but red shifted when shell material is added, consistent with a relaxation of quantum confinement brought on by surrounding the CdSe with a slightly higher bandgap semiconductor instead of capping ligands with enormous HOMO/LUMO gap such as OA or OLA. The spectra match those published by Ithurria and Talapin using the same procedure. In contrast, the CdSe exciton peaks for the CdSe/PbS QDs gradually become washed out and are replaced by a broad, featureless spectrum. There are no peaks or other features in the near IR indicative of PbS excitons. Combined

with the observation of material precipitating during the procedure, the absorption spectra suggest that bulk PbS is simply being formed in solution and not grown on the CdSe cores.

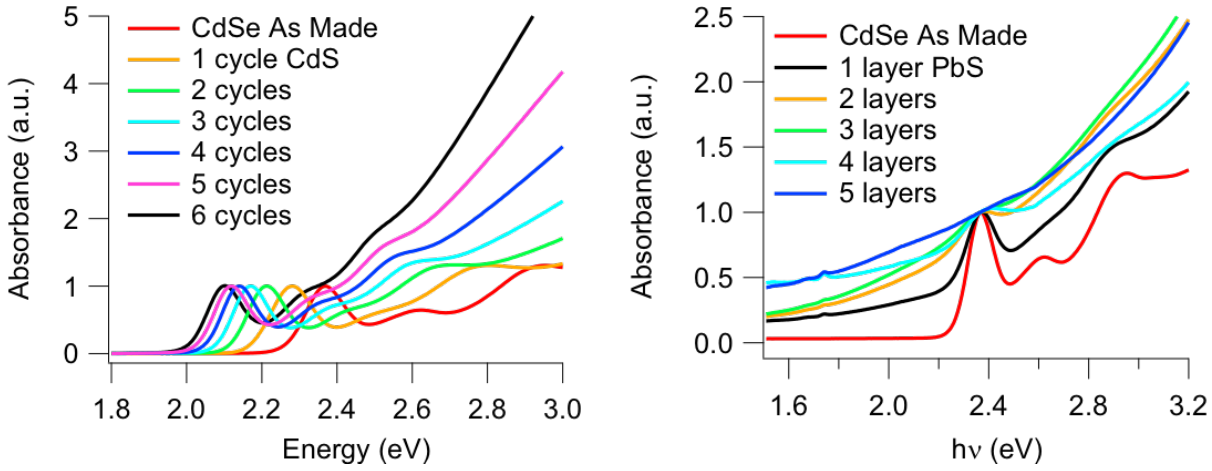

Figure 5. Absorption spectra of CdSe/CdS QDs (left) and CdSe/PbS QDs prepared using solution-phase SILAR. The CdSe/CdS spectra match reported literature reports using the same synthesis and are indicative of successful core/shell structure formation. The CdSe/Pb spectra are suggestive of bulk PbS growth.

Figure 6 shows TEM images of the 6-layer CdSe/CdS sample and the 5-layer CdSe/PbS sample shown above. The CdSe/CdS QDs are clearly larger than the starting 3.5 nm cores and particles with lattice fringes in only the core (right side of left image) or in only the shell (left side of left image) can be identified, reinforcing the evidence that they are true core/shell particles. In the CdSe/PbS sample there is a wide size distribution of nanoparticles, the larger of which appear to be homogeneous PbS (inset of right image) due to their continuous lattice fringes. In is unclear whether the CdSe is amongst the aggregated particles or whether it remains as isolated QDs; the difference in contrast between PbS and CdSe along with the small size of the starting CdSe QDs makes it impossible to see the CdSe QDs amongst the large amount of PbS using this instrument, and the elemental analysis available has too low of resolution to do anything other than identify that both Cd and Pb

are present throughout the sample. Either way, the technique does not form core/shell particles, and neither do any of the synthesis permutations described in the previous section.

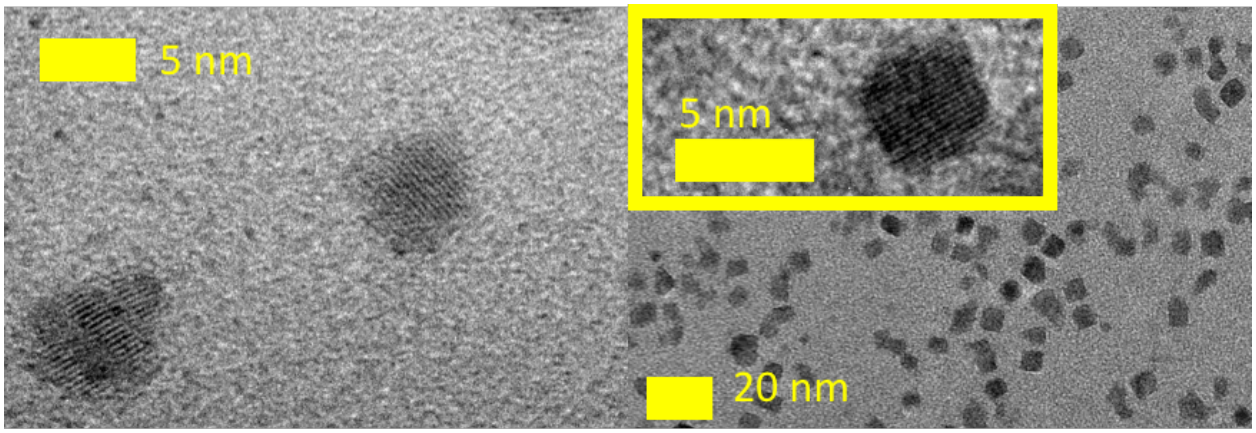

Figure 6. TEM images of CdSe/CdS (left) and CdSe/PbS particles grown via solution-phase SILAR. The left CdSe/CdS particle on has lattice fringes in the shell and the right particle only has lattice fringes in the core, demonstrating that the core and shell are two different materials. The particles in the right image have widespread aggregation, have a widespread size distribution, and have continuous lattice fringes, indicating they are all one material.

One possible explanation for the negative results with the CdSe/PbS particles is that the Pb and S precursors were not being effectively removed from the solution between steps, resulting in homogeneous nucleation of PbS particles. Although this clearly does not occur in the case of CdSe/CdS, it is possible that slight differences in precursor solubility cause the washing step to be ineffective for the Pb precursor (in other words, it is slightly soluble in the nonpolar phase and thus not completely removed). In order to test this hypothesis, the synthesis procedure was repeated without CdSe QDs. This resulted in no formation of any type of material. This means that the precursors are growing on the surface the QDs, but the resulting surface is so thermodynamically unfavorable that the particles either aggregate or the precursors rapidly desorb and react with each other.

Because it appeared that the first cycle of PbS growth maintained the colloidal stability of the QDs, further characterization of this step was performed in order to identify a path forward for the subsequent steps. Figure 7 shows XRD patterns of the starting CdSe cores and the QDs after one cycle of SILAR with PbS. If the QDs were being coated with a monolayer of PbS and not aggregating, there should be no signature of PbS in the XRD pattern because a monolayer of material cannot produce an interference pattern. However, a relatively sharp PbS peak is seen and thus even though they remain colloidally stable, the particles are either aggregating or PbS is desorbing and nucleating. Figure 8 shows TEM images of the same samples. Because OLA and OA are nearly the same size, if the individual QDs were coated with OLA ligands after the SILAR cycle, the inter-particle separation between the two images should be almost identical. The fact that the particles are extremely close together shows that the OLA ligands are not capable of stabilizing the QDs once they have Pb on the surface and so instead they aggregate.

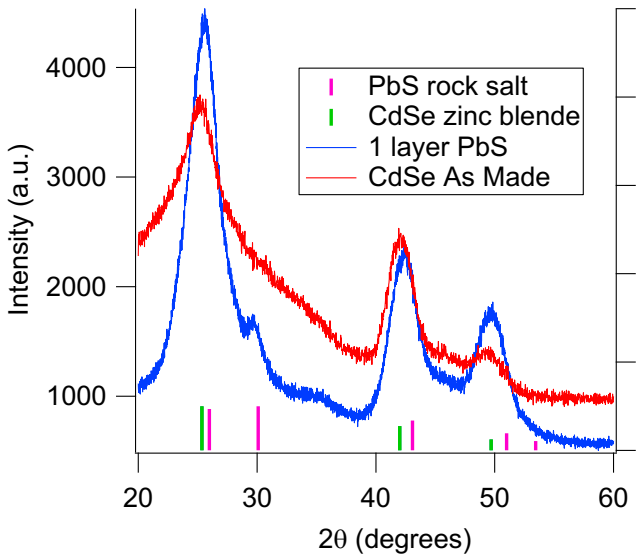

Figure 7. XRD pattern of CdSe QDs before and after one cycle of PbS SILAR. The peak at 30 degrees indicates that PbS has formed beyond one monolayer.

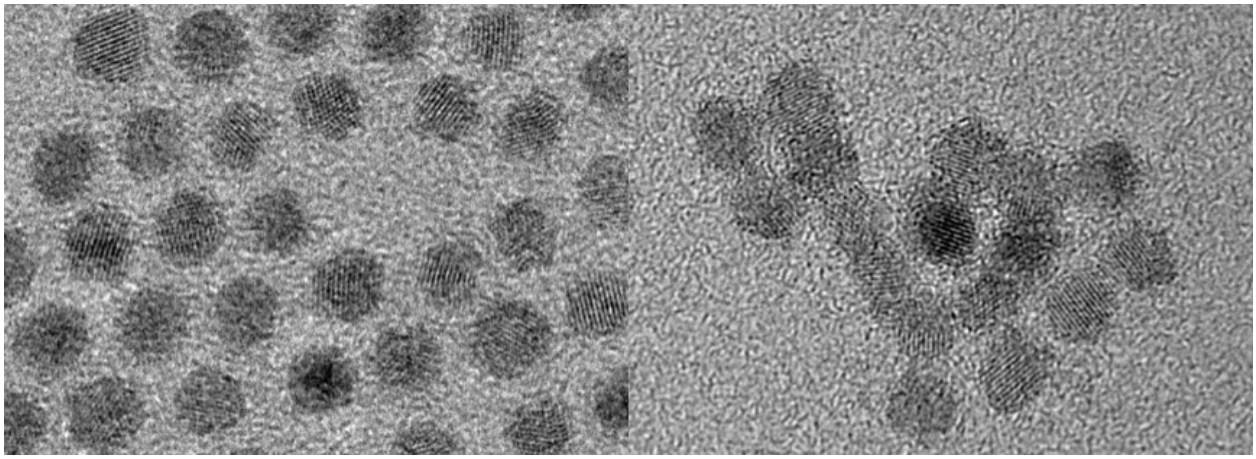

Figure 8. CdSe QDs before (left) and after (right) one PbS SILAR cycle. The SILAR process causes the QDs to aggregate and subsequent cycles cause them to lose their colloidal stability.

Solution-phase SILAR was ultimately unsuccessful at growth CdSe/PbX core/shell QDs because the PbX surfaces are simply too unstable to be effectively passivated regardless of the ligands used. PbX surfaces are much more reactive than CdX surfaces, which is clearly illustrated by the extreme air-instability of PbX QDs compared to the total stability of CdX QDs. It is likely that additional sources of instability from being grown on a CdSe QD surface, such as lattice mismatch, further add to the instability and make the resulting QDs extremely difficult to stabilize. There still have been no demonstrations of colloidal CdX/PbX core/shell QDs despite widespread study of the inverse PbX/CdX structures. The CdX/PbX Janus particles reported by Zhang et al remain the closest result.

2.3 ALD infilling with PbS

The substantial struggles with colloidal approaches to CdX/PbX core/shell structures motivated us to try a solid-state approach. Because the ultimate goal of these materials is to use them in thin film devices, fabricating the desired material structure around already formed QD thin films has numerous advantages. The goal of this portion of the project was

to develop an apparatus and methods to infill a CdX QD thin film with PbS using ALD. If the ALD process is capable of infilling the surrounding area between QDs, the resulting inorganic matrix would have the desired inverse type-II heterostructure and would have a connected pathway of the lower bandgap material. The Law lab possesses a homemade, glovebox-based ALD reactor and has demonstrated the ability to completely infill QD films with oxide materials[25-27]. Most of the key obstacles to this approach described in the following section are related to difficulties with the only available Pb ALD precursor and its compatibility with the reactor.

2.3.1 Reactor design

The ALD reactor used in this work is a homemade cold-wall constant flow reactor built inside a glovebox. ALD precursors are connected to chemical-resistant pneumatic ALD valves that are assembled in a 3x2 geometry around a valve manifold. Constant nitrogen flow of 100 sccm is maintained through the central line of the manifold to ensure downstream flow. The flow path moves from the valve manifold into the spherical reactor chamber (approx.. diameter 15 cm) and out to two chemical-resistant vacuum pumps. A 3-way solenoid valve switches flow between the two pumps to ensure one pump only sees metal precursors and one pump only sees water and H_2S. Samples sit on a flat, heated substrate which can reach 400 C. The walls of the chamber are wrapped with heat tape and can reach 100 C. A Baratron pressure gauge is connected to the main chamber to monitor system pressure. With nitrogen flow, the base pressure of the system is in the range of 80-120 mtorr. The gauge and valves are connected to a logic board which is controlled by LabView software.

In order to perform ALD of PbS, a separate line for Pb precursors had to be added to the system. This is because the only widely studied and commercially available ALD precursor for Pb is lead bis(2,2,6,6-tetramethyl-3,5-heptanedionate) – $Pb(tmhd)_2$ – which is a solid below 134 C and does not have substantial vapor pressure below 140 C[48,49,50]. This means that the entire line leading from the precursor to the chamber (and ideally the chamber itself) must be maintained at 140 C. The other ALD precursors used in the reactor, however, must be kept at room temperature, and the valves controlling their flow have maximum rated temperatures of 65 C. Therefore the line and housing for the Pb precursor had to be attached separately and a high temperature pneumatic valve had to be used to control the precursor flow. The housing for the precursor consisted of a stainless steel tube with compression fittings connecting it to the valve and a removable cap into which an alumina boat containing the precursor was placed. The housing, valve, and line connecting the valve to the chamber were connected to thermocouples and heaters and thus could be maintained at the desired temperature. A schematic of the entire system is shown in Figure 9. The precursor for sulfur was H_2S which was connected to the main valve assembly.

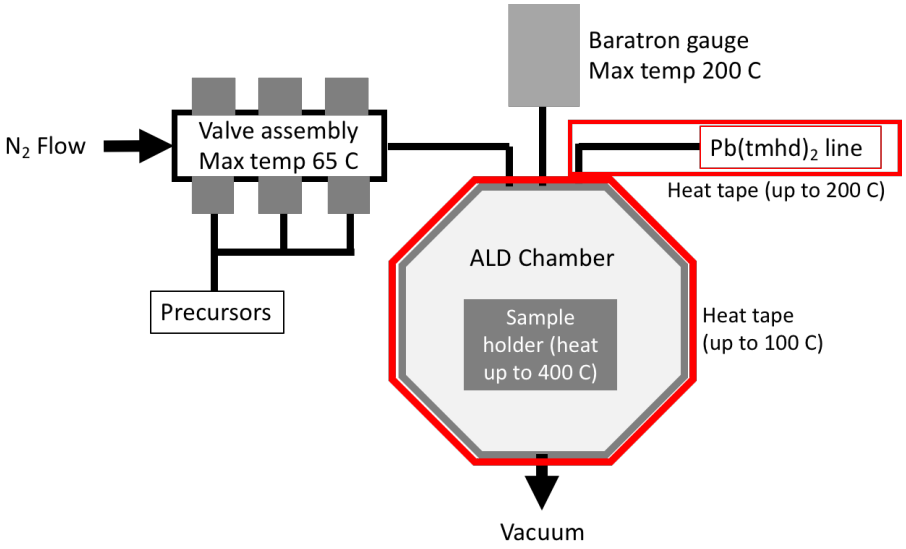

Figure 9. Schematic of the ALD reactor

2.3.2 Characterization of PbS films

Thin films of PbS were grown via ALD and characterized. Films were grown on polished metallic silicon substrates in order to determine the growth rate and verify that ALD growth was occurring (a true layer-by-layer ALD process should have a linear growth rate vs. number of cycles, while CVD growth will generally be nonlinear). Films were also grown on glass to perform XRD and optical characterization. Figure 10 shows SEM top-down images, SEM cross-sections, XRD pattern, and XPS elemental analysis of the resulting films. The growth rate is linear and is approximately 0.5 Å per cycle. The films are phase-pure rock salt PbS (galena) with considerable organic content which is likely left over from the large organic ligands on the Pb precursor. The crystal grains are relatively small – Scherer equation fits to XRD patterns indicate they are 10-15 nm, which is corroborated by SEM.

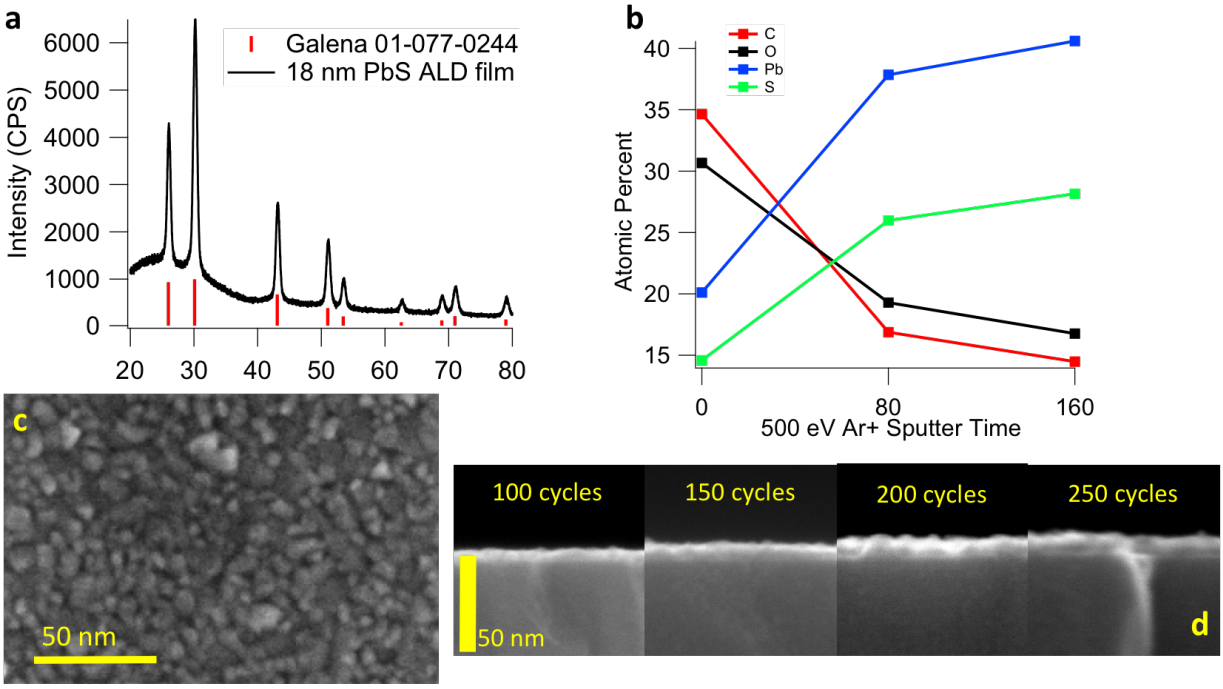

Figure 10. Characterization of PbS films growth via ALD. XRD pattern (a) indicates films are phase pure rock salt PbS. Broad feature at low angle is glass substrate. XPS analysis (b) indicates that there is substantial organic content in films, even after adventitious carbon layer is sputtered off. SEM top-down imaging (c) shows crystal grains are small but films are conformal. SEM cross section imaging (d) establishes linear growth rate of 0.5 Å per cycle

The electronic properties of the PbS films were studied by depositing them on pre-patterned FET substrates. The substrates are planar devices with metallic silicon bottom contacts, 200 nm thick SiO_2 gate layer, and gold top contacts deposited via photolithography with 5, 10, and 25 μm channel widths (one width per substrate for three total devices per substrate) and 1 mm channel length. By depositing ALD films on top of the substrate, the semiconductor fills in the channel and completes the device. Figure 11 shows I/V curves for 40 nm films in the 10 μm channel. FET measurements indicate that the films are p-type with strong current transients consistent with the numerous surface trap states present in such polycrystalline films. Fits to the transfer curves in the linear regime using

the depletion approximation result in a hole mobility of $\mu_h = 0.012\ \mathrm{cm}^2/\mathrm{V} * \mathrm{s}$. These results essentially tell us that the films are behaving as we expect them to: like low purity, low crystallinity semiconductors. They provide a baseline against which future measurements of heterostructures can be compared.

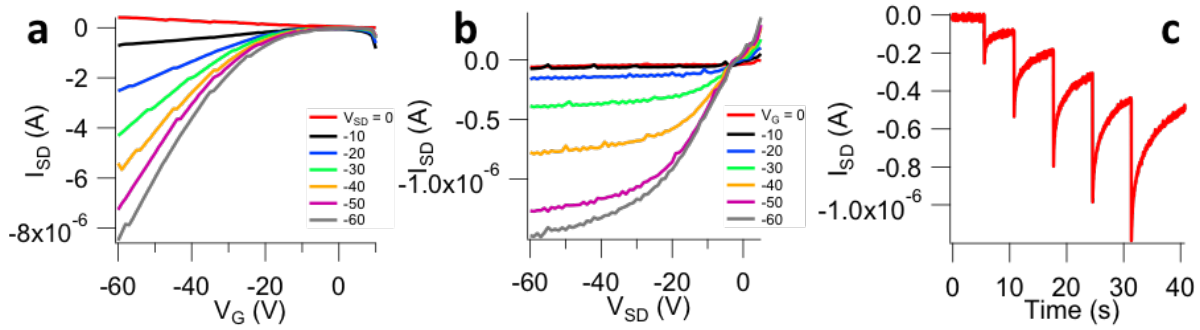

Figure 11. Transfer (a), output (b), and transient (c) I/V curves of FETs with ALD-grown PbS as the active layer. Films are p-type with mobility of $\mu_h = 0.012\ \mathrm{cm}^2/\mathrm{V} * \mathrm{s}$ and strong current transients.

2.3.3 Characterization of PbS/CdSe films

Once ALD growth of PbS was verified, PbS ALD was performed on thin films of CdSe QDs. The films were fabricated by layer-by-layer dipcoating and ligand exchange. In this process, a substrate is immersed in a QD solution and slowly removed using an automated dipcoating device, depositing a monolayer or sub-monolayer on the substrate. Then the sample is immersed in a ligand solution to exchange the native oleate ligands with shorter ligands whose protonated forms are volatile. This is done because previous work has shown that when QD films with these ligands are exposed to H2S inside the ALD chamber, the ligands completely protonate, detach from the dots, and are removed into the vacuum. The only ligand remaining and the QDs is the thiol group from the deprotonated H_2S[51]. This is the ideal scenario for subsequently infilling the QD network with PbS. The two ligands selected were ammonium thiocyanate (NH_4SCN) and formic acid (FA)

After ligand exchange the sample is then immersed in a rinse solution to remove excess ligand, and the process is repeated to build up a film of the desired thickness. Solvents are chosen so that the QDs with oleate ligands are not soluble in the ligand and rinse solutions, and the short ligand-capped QDs are soluble in none of the solvents. This allows the film to continue to build up without QDs coming off. Hexane was used as the QD solvent and acetonitrile was used as the ligand and rinse solvent. Films studied were between 80-100 nm thick. Films of comparable thickness of oleate-capped dots were also made for comparison using a single step spincoating. Films studied optically were made on glass while films studied via XPS were made on polished metallic silicon. After film formation, ALD of PbS was performed on the CdSe QD films. 5 nm of PbS was deposited on the films studied optically while 20 nm was deposited on the films studied by XPS. An optical sample with no CdSe QDs was also prepared for comparison. The first precursor introduced was always H_2S in order to remove the ligands.

Figure 12 shows UV-vis spectra of the optical films before and after ALD for each ligand as well as the QD-free sample. In each case, the first exciton peak from the QD spectrum is preserved after ALD, indicating the QDs are still quantum confined and have not been fused together or otherwise destroyed. The overall absorbance above 1 eV increases in all cases and increases substantially for the oleate-capped film. In fact, the sum of the starting oleate film spectrum and the QD-free PbS spectrum is lower in absorbance than the QD-oleate with ALD spectrum. This strongly suggests that material has been deposited inside the QD network and not just on the surface. Because there is much more surface area to grown on, the total amount of PbS deposited is higher if it is actually infilling the QD film. It was not conclusive from optical measurements whether the SCN and

FA films were infilled. It makes sense that it would be easier to infill the oleate films because there is much more inter-QD distance with these longer ligands (although it is unclear what happens to the OA after H_2S is introduced.)

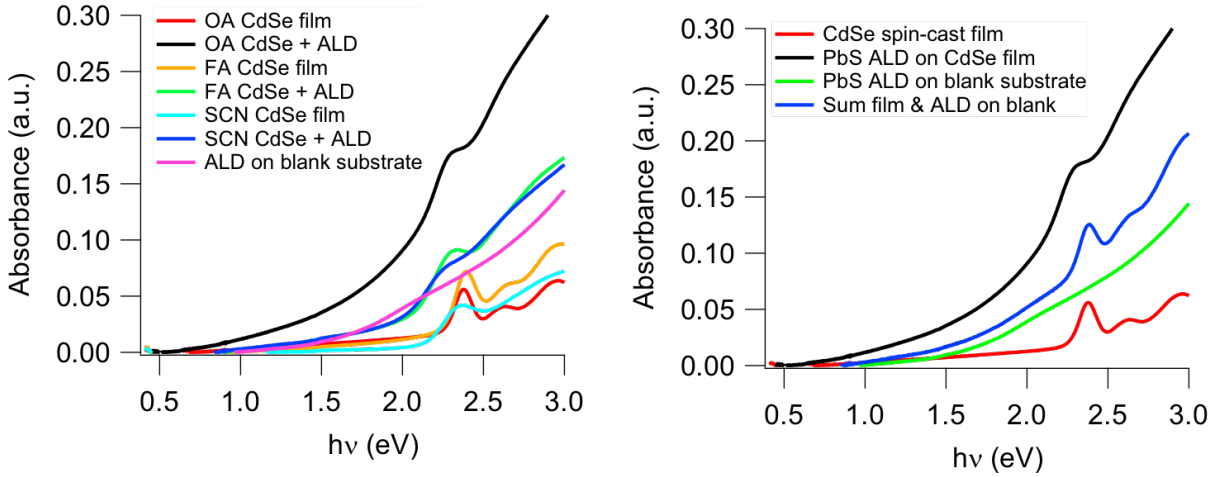

Figure 12. UV-vis spectra of CdSe QD films before and after PbS ALD for all ligands studied (left), showing the excitonic feature of CdSe has been preserved in all cases. Spectra comparing QD-only spectrum, PbS-only spectrum, the sum of those spectra, and the CdSe/PbS spectrum for the oleate-capped QDs (right). The CdSe/PbS absorbance is higher than the sum spectrum, indicating infilling has occurred.

The short ligand films were studied using XPS depth-profiling to attempt to determine whether or not they were infilled or whether to PbS layer was only grown on top of the films. Figure 13 shows the peak area vs sputter cycle (depth) for each element analyzed as well as the peak shape at each cycle for Pb 4f and S 2s/Se 3s for the CdSe-SCN/PbS film. All spectra were corrected to the C 1s line. All reference lines were taken from the NIST XPS database. In the depth profiles, we see an immediate decrease in carbon and an increase in other elements after the first sputter cycle due to the removal of adventitious carbon. During the first few cycles only Pb, S, and C are present as the sputtering moves through the 20 nm overlayer. Once the CdSe films is exposed, Cd and Se signals increase and plateau. The Pb signal decreases but does not go to zero and plateaus

in the same region as the Cd and Se signals. This is a clear indication of successful infilling; the total amount of Pb is lower than the top layer because the analyzed area is no longer homogeneous PbS but Pb is present and in a constant concentration in the bulk of the CdSe film. The S signal does not exhibit this behavior and instead goes to zero steadily throughout the experiment. This is likely due to preferential sputtering of S, which is evident in the development of a lower binding energy shoulder in the Pb spectra corresponding to metallic Pb. This develops even after the first sputter cycle, indicating that the preferential sputtering is quite severe. Additionally, it is difficult to measure the amount of S in these samples because all of the peaks from S overlap with those from Se. The S 2s peak was selected over the much stronger S 2p peak because there is a few eV worth of separation between S 2s and Se 3s, however, even then there is some overlap making it difficult to analyze the S signal. At the end of the depth profile, once the substrate is reached, the Si signal increases and reaches a steady value while all other signals go to zero as expected. It is unclear why there is more carbon within the CdSe/PbS layer; it is possible that although infilling occurs, the ALD process is less complete and so there is more unreacted Pb precursor.

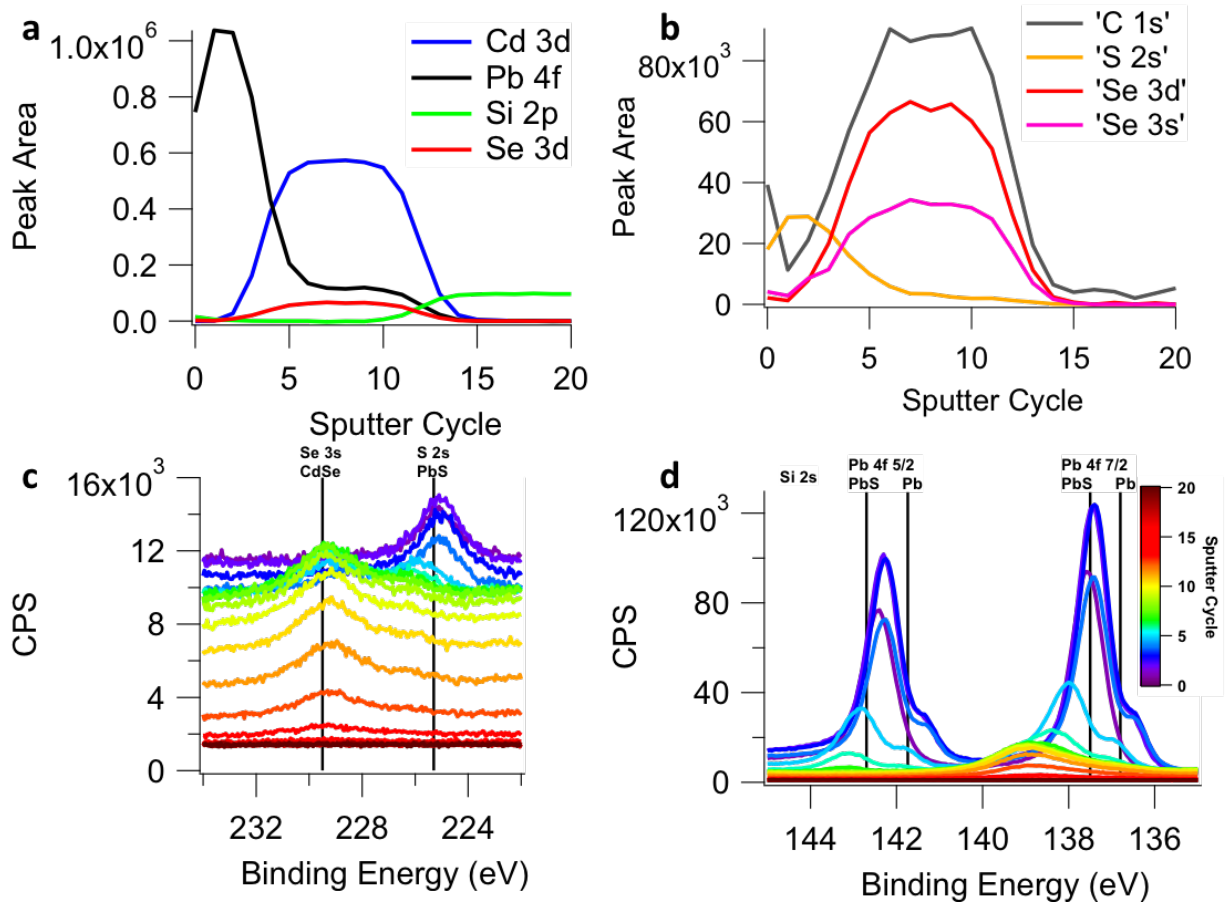

Figure 13. XPS depth profile results from CdSe-SCN films with PbS ALD showing peak area vs. sputter cycle for Cd, Pb, Se, and Si (a) and C, S, and Se (b). The behavior of the Pb peak area in the different layer of the sample indicates that the film is infilled with PbS. XPS specrtra for S 3s and S 2s (c) and Pb 4f (d) for all runs show the partial overlap of S and Se peaks and well as the development of a metallic Pb shoulder indicating the preferential sputtering of S.

The successful infilling of ligand-free CdSe QD films with PbS means that we have successfully formed a CdSe/PbS core/shell heterostructure. Whether this structure behaves in the way that core/shell QDs synthesized colloidally do remains to be seen. The next steps after demonstrating these samples was supposed to be to begin electronic characterization as well as ultrafast optical experiments to measure MEG rates. Unfortunately, the ALD runs that produced the samples shown in this section were the last successful PbS depositions in this reactor, as described in the following section.

2.3.4 Issues with PbS ALD

Throughout the course of the PbS ALD experiments described in the above section, there were numerous difficulties with the ALD system and the success rate for ALD growth of PbS was under 50%. The first issue that became immediately apparent was that it required extremely long pulses of Pb precursor to successfully grow films, to the extent that the precursor would be completely depleted after only a few hundred cycles. If this much material had made it onto the sample there would not be layer-by-layer growth, so it was unclear where the majority of the material was going. Shortly after the XPS depth profile experiments the success rate become zero and ALD of other materials that previously always worked, such as Al_2O_3 also stopped working. This required the entire system to be taken apart, cleaned, and inspected to try to solve the issue (a months-long process). What became immediately apparent was that there was an enormous build-up of material around the outlet of the Pb precursor line into the main chamber. Essentially, because the system was not designed for high-temperature operation, the precursor was condensing on the colder walls of the chamber. Eventually the built up material blocked the path of the precursor to the sample. It also slowly off-gassed and interfered with the deposition of all other materials. No amount of troubleshooting fixed this problem and even after reinstalling the ALD system, ALD of other materials was less consistent than it used to be and ALD of PbS was unsuccessful. The system was simply not designed for high temperature precursors. It was probably sheer luck that any successful samples were made at all. The fabrication of a new, high temperature system was planned but not completed.

2.4 Conclusion

Synthesizing CdX/PbX core/shell QDs via chemistries used to synthesize other core/shell QDs appears to be an intractable problem. The PbX surface is simply too unstable to be stabilized by SILAR methods and the seeded growth mechanism of the cation exchange reaction prevents the desired core/shell structure from forming. I have demonstrated that forming CdX/PbS heterostrucutres by infilling CdX QD films with ALD in possible. Doing so reliably requires an ALD reactor that is compatible with high-temperature precursors. There is an enormous amount of characterization and optimization to be done if such a system can be used to make samples. The successful fabrication of such a custom, glovebox-based, high temperature ALD system will enable an exciting avenue of future work.

3 Charge transport studies in high performance PbS QD films

Although the Cd to Pb partial cation exchange synthesis does not form core/shell QDs, the resulting PbX QDs that are formed when the complete exchange reaction occurs have unique properties. Most notably, these QDs are indefinitely air-stable as synthesized which no other PbX synthetic route has been able to achieve. The explanation for this behavior is that the chloride ions present in the reaction help passivate the QD surfaces, as does the residual Cd left on the QDs after the exchange reaction. This synthesis was developed by our collaborators at the National Renewable Energy Laboratory (NREL). They also developed a facile, ambient condition processing method to fabricate thin films with these QDs that produced solar cells with high efficiencies[52]. Interestingly, the high performance in these devices does not appear until the devices are stored in air for a day or two; when the devices are initially measured they have low efficiency. As part of our collaborative Energy Frontier Research Center (EFRC), the various labs in the center used a variety of techniques to better understand these QD films, ultimately resulting in a submitted manuscript. The following is my contribution to that effort. It consists of a series of FET measurements and characterization using XPS and UPS in order to understand what air exposure actually does to the films and why the devices "turn on" after storage in air for 24-48 hours.

3.1 Film fabrication

PbS QDs were synthesized at NREL using the same procedure as the complete cation exchange reaction described in Section 2.1.2, except 3.2 nm diameter CdS QDs were used as the starting QD seeds. The resulting PbS QDs had a first exciton absorption peak at 950 nm. When implemented as the active layer in solar cells, these QDs are deposited in several

spin-coating and ligand exchange steps. For each step, an approximately 75 nm layer of QDs is spincoated onto the substrate, then the device is soaked in a ligand solution for 1 minute, then rinsed with solvent and dried with compressed nitrogen. The first four layers of the device use 10 mM PbI_2 in DMF as the ligand solution and acetonitrile as the rinse solvent. The last two layers use 10% 3-mercaptopropionic acid (MPA) in methanol as the ligand solution and methanol as the rinse solution. The final films are annealed in a glovebox as 120 C for 20 min.

The films implemented in FETs and studied with XPS/UPS used single spincoated layers with three distinct ligand treatments. The first two treatments were simply the PbI_2 and MPA treatments described above. The third treatment consisted of the PbI_2 treatment followed by the MPA treatment. The purpose of this specific treatment was to mimic the fact that in the 6-layer solar cell stacks, the layers that have received the PbI_2 treatment are at least partially exposed to MPA when the subsequent layers above them get treated. It is quite possible that this occurs in a gradient, where the topmost PbI_2 QDs see the most MPA and the bottom QDs the least. All films received the 120 C anneal in the glovebox. Samples were made for each of the three treatments and half of them were kept in the glovebox at all times (but still fabricated in air) and half of them were stored in ambient conditions. The FET substrates were the same substrates described in Section 2.3.2 while the XPS/UPS samples were deposited on polished metallic silicon substrates. The air-free XPS/UPS samples were transferred into the lab to the instrument in a sealed vacuum flange and brought into the instrument through a glovebox load-lock and thus never were exposed to air.

3.2 Oxidation study using FETs

FET measurements were carried out on each set of samples using the 10 μm channel. Transfer and output curves were measured at a scan rate of 60 V/s, which was the fastest possible scan rate with acceptable signal to noise ratio. Linear mobilities were calculated from transfer curves acquired at V_{SD} = ±10 V (with positive VSD for electrons and negative VSD for holes), according to the gradual channel approximation equation in the linear regime. The slope of the transfer curves for linear mobility calculations was measured at V_G = ±50 V. All samples exhibited severe current transients and thus the calculated mobility values are likely underestimated. Measurement results are shown in Figure 14 and the calculated mobility values are summarized in Table 1.

Table 1. FET Mobility values

Ligand	**PbI_2**	**MPA**	**PbI_2/MPA**
Mobility (pristine, n-channel) ($cm^2/V*s$)	1.3×10^{-4}	5.8×10^{-4}	2.6×10^{-3}
Mobility (air-exposed, p-channel) ($cm^2/V*s$)	8.8×10^{-6}	5.8×10^{-6}	1.8×10^{-5}

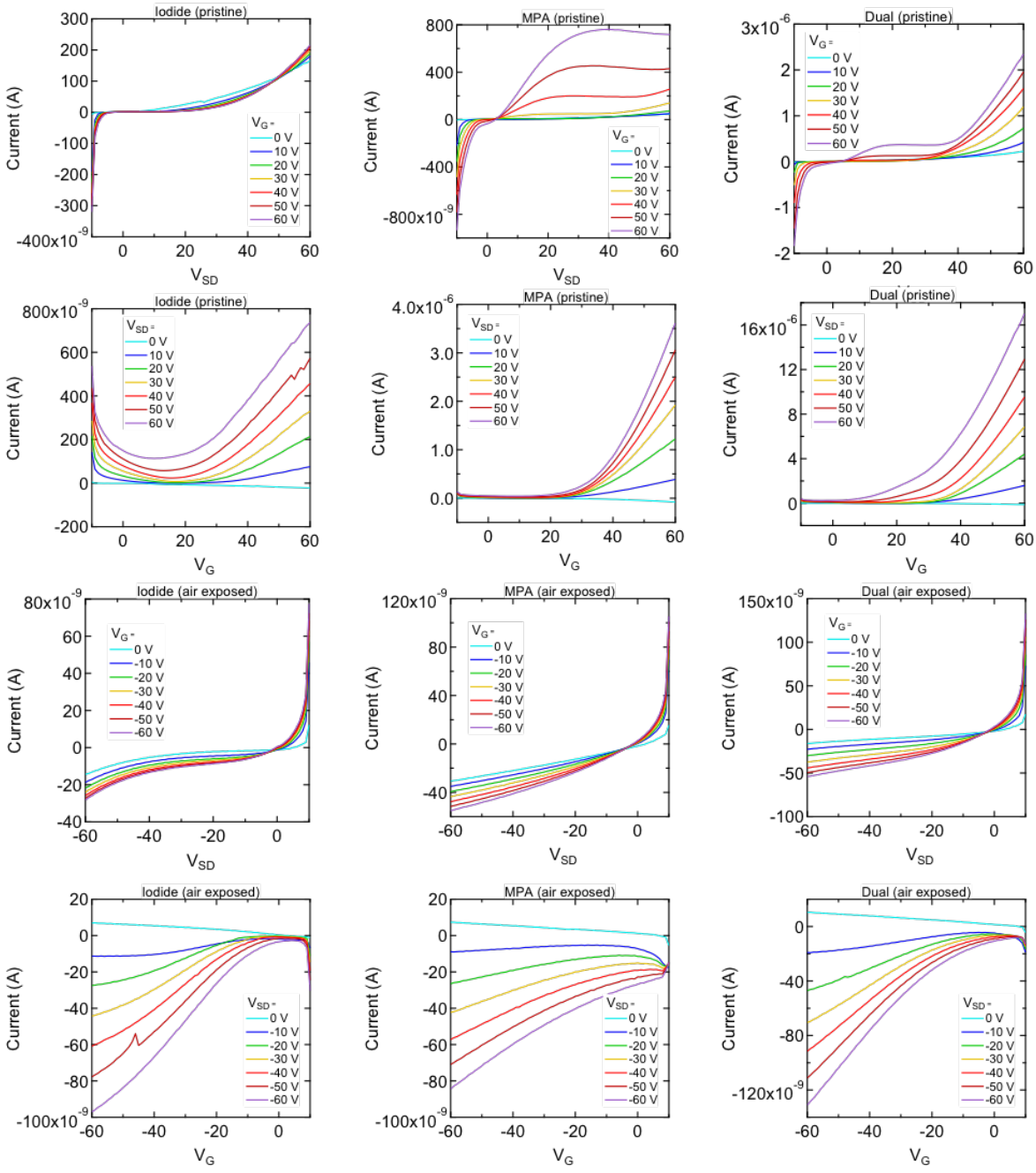

Figure 14. Output (rows 1 & 3) and transfer curves (rows 2 & 4) for iodide (left), MPA (center), and dual (right) treated QD films stored in the glovebox (top half) and stored in air (bottom half). In each case, QDs transition from n-channel to p-channel following air exposure.

For each treatment, the devices are initially n-channel and transition to p-channel with a substantial decrease in mobility after air exposure. It is hypothesized that one of the reasons the solar cells fabricated from these films are efficient is that the iodide layer is n-type while the MPA layer is p-type which creates a heterojunction within the active layer as assists charge separation. Although all of the films studied here were p-type after air exposure, it is possible that the lower iodide-treated layers in the solar cell stacks are buried deep enough that oxygen cannot diffuse far enough to reach them, and thus they remain n-type, or at least that there is a Fermi level gradient across the stack that behaves like a heterojunction. It could also be possible that the hypothesis is wrong and that all of the layers become p-type. In that case the boost in performance could be due to better band alignment with the underlying TiO_2 layer that is used in the device stack.

3.3 Carrier type determination using XPS/UPS

To better understand and quantify the changes in carrier type after air exposure, band-edge XPS and UPS measurements were conducted on each of the film types and fit to calculate the location of the Fermi level with respect to the valence band minimum (VBM). Measurements were calibrated to the cutoff energy of the instrument's internal silver standard. The results are shown in Figure 15.

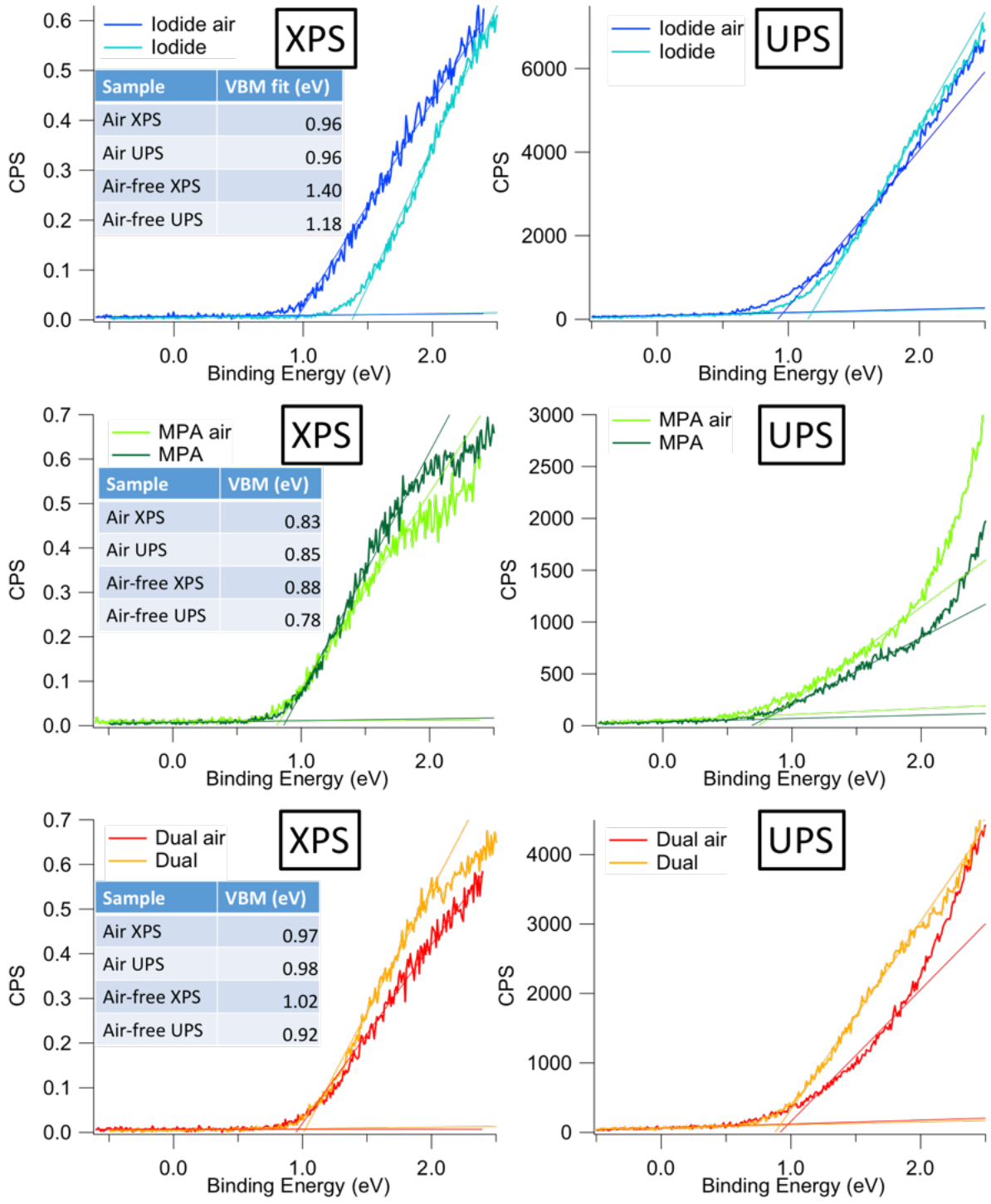

Figure 15. VBM measurements of iodide (top), MPA (center), and dual (bottom) treated films using XPS (left) and UPS (right). Calculated values for VBM vs. E_F are shown in insets.

Interestingly, the results differ somewhat from the FET results and the XPS and UPS results do not agree. It is possible that the hard UV photons caused photo-oxidation of the films, resulting in values similar to the XPS values for both air-free and air-exposed films. The UPS measurements were in general less reproducible so the XPS results were deemed more reliable. The QDs had a bandgap of roughly 1.3 eV, so all of the calculated values for the VMB/ E_F distance would correspond to n-type materials, however there is considerable band tailing seen in the spectra and the measurement error is a few tenths of an eV so it is not particularly useful to look at the exact numerical values. Instead, looking at the differences between samples gives some insight into the film behavior. Before air exposure, the iodide-treated films have the highest Fermi level, followed by the dual treated films and then the MPA films. After air exposure, the iodide films shift drastically to lower Fermi level while the MPA and dual films shift slightly. The iodide and dual have roughly the same Fermi level position while the MPA position is lower. It could be the case that although the Fermi level gradient is present even before air exposure, the air exposure is needed to push the MPA film from n-type to p-type while the iodide and dual treated films remain n-type or ambipolar, thus establishing the desired heterojunction.

3.4 Conclusions

I have explored the electronic properties of high performance PbS QD thin films in order to better understand why they function well in solar cells. FET and XPS measurements clearly indicate that there is a shift in carrier type from more n-type to more p-type, although the exact band alignment in still unclear. Because the solar cells perform well only after air exposure, we can generally conclude that somehow this shift creates a favorable band alignment that is needed for the devices to work. After about two days of

storage in air, the properties of the films stay constant indefinitely. Considering the fact that the as-made QDs are indefinitely air-stable, the air-induced changes in the films may be due to phenomena occurring with the ligands and not the QDs themselves. Either way, the ability to fabricate high performance, air-stable QD devices is a promising step forward.

References

[1] Cardona, M.; Peter, Y. Y. Fundamentals of Semiconductors. Springer **2005**.

[2] Luttinger, J.; Kohn, W. Motion of Electrons and Holes in Perturbed Periodic Fields. Phys. Rev. **1955**, 97, 869883.

[3] Kane, EO Band Structure of Indium Antimonide. Journal of Physics and Chemistry of Solids **1957**, 1(4), 249-261

[4] Ekimov, AI; Hache, F; Schanne-Klein, MC; Ricard, D Absorption and Intensity-Dependent Photoluminescence Measurements on CdSe Quantum Dots: Assignment of the First Electronic Transitions. JOSA B **1993**, 10, 100-107

[5] Wise, F. Lead Salt Quantum Dots: The Limit of Strong Quantum Confinement. Accounts of Chemical Research **2000**, 33, 773-780

[6] Kang, I; Wise, FW Electronic Structure and Optical Properties of PbS and PbSe Quantum Dots. JOSA B **1997**, 14(7), 1632-1646

[7] Beattie, AR; Landsberg, PT Auger Effect in Semiconductors. Proceedings of the Royal Society of London A **1959**, 249

[8] Shockley, W.; Queisser, H. J. Detailed Balance Limit of Efficiency of P N Junction Solar Cells. Journal of Applied Physics **1961**, 32, 510–519.

[9] Nozik, AJ Multiple Exciton Generation in Semiconductor Quantum Dots. Chemical Physics Letters **2008**, 457(1), 3-11

[10] Urayama, J; Norris, TB; Singh, J; Bhattacharya, P Observation of Phonon Bottleneck in Quantum Dot Electronic Relaxation. Physical Review Letters **2001**, 86(21), 4930-4933

[11] Chepic, DI; Efros, AL; Ekimov, AI; Ivanov, MG Auger Ionization of Semiconductor Quantum Drops in a Glass Matrix. Journal of Luminescence **1990**, 47, 113-127

[12] Efros, A. L.; Efros, A. L. Interband absorption of light in a semiconductor sphere, SoV. Phys. Semiconductors **1982**, *16*, 772.

[13] Burda, C; Chen, X; Narayanan, R; El-Sayed, MA Chemistry and Properties of Nanocrystals of Different Shapes. Chemical reviews **2005**, 105, 1025-1102

[14] Fu, H; Tsang, SW Infrared Colloidal Lead Chalcogenide Nanocrystals: Synthesis, Properties, and Photovoltaic Applications. Nanoscale **2012**, 4, 2187-2201

[15] Čapek, R.; Yanover, D.; Lifshitz, E. Size Control by Rate Control in Colloidal PbSe Quantum Dot Synthesis. Nanoscale **2015**, Advance Article

[16] Brown, PR; Kim, D; Lunt, RR; Zhao, N; Bawendi, MG Energy Level Modification in Lead Sulfide Quantum Dot Thin Films through Ligand Exchange. ACS Nano **2014**, 8(6), 5863–5872

[17] Zhang, H; Jang, J; Liu, W; Talapin, DV Colloidal Nanocrystals with Inorganic Halide, Pseudohalide, and Halometallate Ligands. ACS Nano **2014**, *8*(7), 7359–7369

[18] Nag, A; Kovalenko, MV; Lee, JS; Liu, W Metal-Free Inorganic Ligands for Colloidal Nanocrystals: S2–, HS–, Se2–, HSe–, Te2–, HTe–, TeS32–, OH–, and NH2–as Surface Ligands. Journal of the American Chemical Society **2011**, *133*(27), 10612–10620

[19] Ihly, R; Tolentino, J; Liu, Y; Gibbs, M; Law, M The Photothermal Stability of PbS Quantum Dot Solids. ACS nano **2011**, *5*, 8175-8186

[20] Zhang, J.; Gao, J.; Miller, E. M.; Luther, J. M.; Beard, M. C. Diffusion-Controlled Synthesis of PbS and PbSe Quantum Dots with in Situ Halide Passivation for Quantum Dot Solar Cells. ACS nano **2013**, 8, 614–622.

[21] Ning, Z; Ren, Y; Hoogland, S; Voznyy, O All-Inorganic Colloidal Quantum Dot Photovoltaics Employing Solution-Phase Halide Passivation. Advanced Materials **2012**, 24, 6295-6299

[22] Bae, WK; Joo, J; Padilha, LA; Won, J Highly Effective Surface Passivation of PbSe Quantum Dots through Reaction with Molecular Chlorine. Journal of the American Chemical Society **2012**, 134 (49), 20160-20168

[23] Zhang, J.; Gao, J.; Church, C.; Miller, E.; Luther, J.; Klimov, V.; Beard, M. PbSe Quantum Dot Solar Cells with More than 6% Efficiency Fabricated in Ambient Atmosphere. Nano Letters **2014**, 14 (10), 6010-6015

[24] Ip, AH; Thon, SM; Hoogland, S; Voznyy, O Hybrid Passivated Colloidal Quantum Dot Solids. Nature Nanotechnology **2012**, 7, 577-582.

[25] Liu, Y; Gibbs, M; Perkins, CL; Tolentino, J; Law, M Robust, Functional Nanocrystal Solids by Infilling with Atomic Layer Deposition. Nano Letters **2011**, 11, 5349-5355

[26] Liu, Y; Tolentino, J; Gibbs, M; Ihly, R; Perkins, CL; Liu, Y; Law, M PbSe Quantum Dot Field-Effect Transistors with Air-Stable Electron Mobilities above 7 cm2 V−1 s−1. Nano Letters **2013**, 13, 1578-1587

[27] Ten Cate, S; Liu, Y; Sandeep, S. C.; Law, M Activating Carrier Multiplication in PbSe Quantum Dot Solids by Infilling with Atomic Layer Deposition. The Journal of Physical Chemistry **2013**, *4*, 1766-1770

[28] Osedach, TP; Zhao, N; Andrew, TL; Brown, PR Bias-Stress Effect in 1, 2-Ethanedithiol-Treated PbS Quantum Dot Field-Effect Transistors. ACS Nano **2012**, 6(4), 3121-3127

[29] McGuire, J. A.; Sykora, M.; Joo, J.; Pietryga, J. M.; Klimov, V. I. Apparent versus True Carrier Multiplication Yields in Semiconductor Nanocrystals. Nano letters **2010**, 10, 2049–2057.

[30] Stewart, J. T.; Padilha, L. A.; Bae, W.; Koh, W.-K.; Pietryga, J. M.; Klimov, V. I. Carrier Multiplication in Quantum Dots within the Framework of Two Competing Energy Relaxation Mechanisms. The Journal of Physical Chemistry Letters **2013**, 4, 2061–2068.

[31] Ravindra, NM; Srivastava, VK Properties of PbS, PbSe, and PbTe. physica status solidi (a) **1980**, 58(1), 311-316

[32] Padilha, LA; Stewart, JT; Sandberg, RL Carrier Multiplication in Semiconductor Nanocrystals: Influence of Size, Shape, and Composition. Accounts of Chemical Research **2013**, *46*(6), 1261-1269.

[33] Cirloganu, CM; Padilha, LA; Lin, Q; Makarov, NS Enhanced Carrier Multiplication in Engineered Quasi-Type-II Quantum Dots. Nature Communications **2014**, 5

[34] Haas, D. M.; Warman, JM Photon-Induced Molecular Charge Separation Studied by Nanosecond Time-Resolved Microwave Conductivity.Chemical Physics **1982**, 73, 35-53
[35] Sandeep, C.; Cate, T. S.; Schins, JM High Charge-Carrier Mobility Enables Exploitation of Carrier Multiplication in Quantum-Dot Films. Nature Communications **2013**, 4
[36] Ten Cate, S; Sandeep, C.; Liu, Y; Law, M Generating Free Charges by Carrier Multiplication in Quantum Dots for Highly Efficient Photovoltaics. Accounts of Chemical Research **2015**,
[37] Luther, JM; Law, M; Beard, MC; Song, Q; Reese, MO Schottky Solar Cells Based on Colloidal Nanocrystal Films. Nano Letters **2008**, 8(10), 3488-3492
[38] Pattantyus-Abraham, AG; Kramer, IJ; Barkhouse, AR Depleted-Heterojunction Colloidal Quantum Dot Solar Cells. ACS Nano **2010**, 4(6), 3374–3380
[39] Brown, PR; Lunt, RR; Zhao, N; Osedach, TP Improved Current Extraction from ZnO/PbS Quantum Dot Heterojunction Photovoltaics Using a MoO3 Interfacial Layer. Nano Letters **2011**, *11*(7), 2955–2961
[40] Chuang, C.; Brown, PR; Bulović, V; Bawendi, MG Improved Performance and Stability in Quantum Dot Solar Cells through Band Alignment Engineering. Nature materials **2014**, 13, 796-801
[41] Tang, J; Liu, H; Zhitomirsky, D; Hoogland, S; Wang, X Quantum Junction Solar Cells. Nano Letters **2012**, 12, 4889-4894.
[42] Liu, M; Voznyy, O; Sabatini R; García de Arquer, F. P; Munir, R; Balawi, A.H; Lan, X; Fan, F; Walters, G; Kirmani, A.R; Hoogland, S; Laquai, F; Amassian A; Sargent, E.H. *Nature Materials* **2017**, 16, 258–263
[43] Sanehira, E. M., Marshall, A. R., Christians, J. A., Harvey, S. P., Ciesielski, P. N., Wheeler, L. M., ... & Luther, J. M. (2017). *Science advances*, **2017,** *3*(10).
[44] Semonin, OE; Luther, JM; Choi, S; Chen, HY; Gao, J Peak External Photocurrent Quantum Efficiency Exceeding 100% via MEG in a Quantum Dot Solar Cell. Science **2011**, 334, 1520-1533
[45] Ithurria, S.; Talapin, D. Colloidal Atomic Layer Deposition (c-ALD) Using Self-Limiting Reactions at Nanocrystal Surface Coupled to Phase Transfer between Polar and Nonpolar Media. *J. Am. Chem. Soc*. **2012**, *134* (45), 18585–18590
[46] Pu, C.; Zhou, J.; Lai, R.; Niu, Y.; Nan, W.; Peng, X. Highly Reactive, Flexible yet Green Se Precursor for Metal Selenide Nanocrystals: Se-Octadecene Suspension (Se-SUS). *Nano Research* **2013**, 6, 652–670
[47] Zhang, J.; Chernomordik, B. D.; Crisp, R. W.; Kroupa, D. M.; Luther, J. M.; Miller, E. M.; Gao, J.; Beard, M. C. Preparation of Cd/Pb Chalcogenide Heterostructured Janus Particles via Controllable Cation Exchange. *ACS nano* **2015**, 9, 7151–7163.
[48] Krisyuk, VV; Turgambaeva, AE Volatile Lead β-Diketonates as CVD Precursors. *Chemical Vapor* … **1998**.
[49] Dasgupta, NP; Lee, W; Prinz, FB Atomic Layer Deposition of Lead Sulfide Thin Films for Quantum Confinement. *Chemistry of Materials* **2009**.
[50] Dasgupta, NP; Jung, HJ; Trejo, O; McDowell, MT Atomic Layer Deposition of Lead Sulfide Quantum Dots on Nanowire Surfaces. *Nano Letters* **2011**.
[51] Tolentino, J Designing quantum dot solid for optoelectronic devices through matrix engineering. Dissertation, University of California Irvine, **2015**

[52] Kim, S; Marshall, AR; Kroupa, DM; Miller, EM; ACS … L.-J. Air-Stable and Efficient PbSe Quantum-Dot Solar Cells Based upon ZnSe to PbSe Cation-Exchanged Quantum Dots. *ACS Nano* **2015**.